

SRGE J194401.8+284452 — AN X-RAY CATAclySMIC VARIABLE IN THE FIELD OF THE GAMMA-RAY SOURCE 4FGL J1943.9+2841

A. I. Kolbin^{1,2,9*}, A.V. Karpova⁴, M.V. Suslikov^{1,2}, I.F. Bikmaev^{2,3},
M.R. Gilfanov^{5,6}, I.M. Khamitov², Yu.A. Shibano⁴, D.A. Zyuzin⁴, G.M. Beskin^{1,2},
V.L. Plokhotnichenko¹, A.G. Gutaev^{1,2}, S.V. Karpov⁸, N.V. Lyapsina¹, P.S. Medvedev⁵,
R.A. Sunyaev^{5,6}, A.Yu. Kirichenko^{7,4}, M.A. Gorbachev², E.N. Irtuganov², R.I. Gumerov²,
N.A. Sakhibullin^{2,3}, E.S. Shablovinskaya¹, E.A. Malygin¹

¹Special Astrophysical Observatory of RAS, Nizhnij Arkhyz, Karachai-Cherkessian Republic, 369167, Russia

²Kazan (Volga-region) Federal University, Kremlevskaya 18, Kazan 420008, Russia

³Tatarstan Academy of Sciences, Bauman 20, Kazan 420111, Russia

⁴Ioffe Institute, Politekhnikeskaya 26, St. Petersburg 194021, Russia

⁵Space Research Institute, Russian Academy of Sciences, Profsoyuznaya 84/32, 117997 Moscow, Russia

⁶Max Planck Institute for Astrophysics, Karl-Schwarzschild-Strasse 1, Garching bei München D-85741, Germany

⁷Instituto de Astronomía, Universidad Nacional Autónoma de México, Apdo. Postal 877, Ensenada, Baja California 22800, México

⁸CEICO, Institute of Physics, Czech Academy of Sciences, Prague 18221, Czech Republic

⁹North Caucasian Federal University, Pushkina 1, Stavropol 355017, Russia

SRGe J194401.8+284452 is the brightest point-like X-ray object within the position uncertainty ellipse of an unidentified γ -ray source 4FGL J1943.9+2841. We performed multi-wavelength spectral and photometric studies to determine its nature and possible association with the γ -ray source. We firmly established its optical counterpart with the Gaia based distance of about 415 pc. Our data show that the object is a cataclysmic variable with an orbital period of about 1.5 hours. SRGe J194401.8+284452 exhibits fast spontaneous transitions between the high and low luminosity states simultaneously in the optical and X-rays, remaining relatively stable between the transitions on scales of several months/years. This can be caused by an order of magnitude changes in the accretion rate. The brightness of the source is about 17 and 20 mag in optical range and about 5×10^{-12} and 5×10^{-13} erg/cm²/s in the 0.3 – 10 keV range in the high and low states, respectively. We constrained the mass of the white dwarf (0.3 – 0.9 M_{\odot}) and its temperature in the low state (14750 ± 1250 K), the mass of the donor star ($\leq 0.08 \pm 0.01 M_{\odot}$). In the low state, we detected regular optical pulsations with an amplitude of 0.2 mag and a period of 8 min. They are likely associated with the spin of the white dwarf, rather than with its non-radial pulsations. In the high state, the object demonstrates only stochastic optical brightness variations on time scales of 1 – 15 minutes with amplitudes of 0.2 – 0.6 mag. We conclude, that SRGe J194401.8+284452 can be classified as an intermediate polar, and its association with the γ -ray source is very unlikely.

an accretion disk around the white dwarf.

Key words: stars – cataclysmic variables, white dwarfs; X-ray sources; methods – photometry, spectroscopy

INTRODUCTION

The X-ray source XMMSL2 J194402.0+284451 (hereinafter J1944) from the *XMM-Newton* catalog (Saxton, et al., 2008) has the observed flux $f_X = (1.25 \pm 0.45) \times 10^{-11}$ erg s⁻¹ cm⁻² in the 0.2 – 12 keV range according to data from May 3, 2013. It was previously discovered in the *ROSAT* all-sky

survey (Boller, et al., 2016), in which this source is designated as 2RXS J194401.4+284456 (53 counts were obtained in 387 sec in October 1990). The nature of J1944 has not yet been established.

Torres, et al. (2019) suggested that the source is a pulsar wind nebula (PWN) candidate. Its optical counterpart was also identified by positional coincidence with a star from the *Gaia* catalog with

*E-mail: kolbinalexander@mail.ru

a brightness of $G = 17.6^m$. According to the results of X-ray and ultraviolet (UV) observations with the *Swift* telescope in 2018 (with exposure time of 850 sec), the source was too faint to be a PWN, and the question about its nature remained open.

In the subsequent work by Takata, et al. (2022) J1944 was considered as a possible cataclysmic variable (CV). The authors used optical data from the TESS telescope, but they were unable to determine the parameters of the proposed binary to confirm this hypothesis.

Alternatively, J1944 might be a counterpart of an unassociated γ -ray source 4FGL J1943.9+2841. The detection significance of the latter is only $\approx 6\sigma$ and no brightness variability was detected. Its γ -ray flux is $F_\gamma = (4.3 \pm 1.1) \times 10^{-12} \text{ erg s}^{-1} \text{ cm}^{-2}$ in the 0.1 – 100 GeV range and its spectrum can be described by the LogParabola model (Abdollahi, et al., 2022; Ballet, et al., 2023). J1944 is the brightest X-ray source in the ellipse, corresponding to the 95% position uncertainty of 4FGL J1943.9+2841 (Fig. 1). If the identification of J1944 with the γ -ray source is confirmed, it could be a pulsar in a binary system.

To clarify the nature of J1944, we examined X-ray data from the eROSITA telescope (Predehl, et al., 2020) on board the Spektr-RG observatory (SRG; Sunyaev, et al., 2021) obtained during the all-sky scanning in 2020–2021 (the corresponding source name is SRGe J194401.8+284452), optical data from various catalogs and archival UV and X-ray data from *Swift* observations (name in the *Swift*-XRT Point Source catalog – 2SXPS J194401.7+284450, Evans, et al. 2020). Optical spectroscopic and photometric observations were also carried out with the 6-m BTA telescope, the 1.5-m Russian-Turkish telescope RTT-150 and the 2.1-m telescope of the Mexican National Astronomical Observatory (Observatorio Astronómico Nacional San Pedro Mártir, OAN-SPM). Here we present the results of the analysis of these data.

OBSERVATIONS AND DATA REDUCTION

Optical data from catalogs

The parameters of the J1944 optical counterpart candidate, taken from the *Gaia* catalog (*Gaia* Collaboration, et al., 2016, 2023), are presented in Table 1. We found the source in the Isaac Newton Telescope Photometric H-Alpha Survey (IPHAS; Barentsen, et al., 2014), where its apparent magnitudes are $r = 19.60(2)^m$, $i = 19.54(6)^m$ and $H\alpha = 18.41(2)^m$ in the AB photometric system on

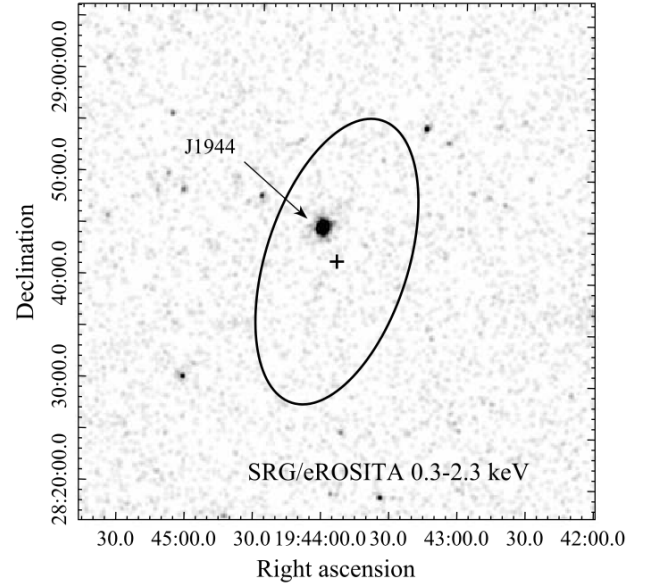


Fig. 1. $50' \times 50'$ eROSITA image of the J1944 field in the 0.3 – 2.3 keV range. The position of the γ -ray source 4FGL J1943.9+2841 is marked with a cross and the ellipse shows its 95% uncertainty (Abdollahi, et al., 2022).

MJD 53563.

There are also IPHAS observations on MJD 54284 and 54674, but their results were not included in the survey, possibly due to non-photometric weather conditions. However, analyzing the corresponding images we found that on these dates the source had approximately the same brightness as in observations on MJD 53563. The best signal-to-noise ratio was obtained in observations on MJD 54674 and we calculated its magnitudes of $r = 19.90(4)^m$ and $H\alpha = 18.66(4)^m$.

In addition, we used data from the Panoramic Survey Telescope and Rapid Response System (Pan-STARRS; Flewelling, et al., 2020) and Zwicky Transient Facility catalogs (ZTF; Masci, et al., 2019) which show significant brightness variability of the source.

Optical photometry

Photometric observations of the J1944 optical counterpart candidate were carried out in the g , r , i and z filters on 2022, 2023 and 2024 with the 1.5-m Russian-Turkish telescope RTT-150 (TÜBİTAK National Observatory, Antalya, Turkey). The telescope was equipped with a TFOSC instrument and an Andor iKon-L 936 BEX2-DD-9ZQ CCD with a size of 2048×2048 pixels, thermoelectrically cooled to -80 C° . The field of view in the direct image mode is $11' \times 11'$

Таблица 1. Parameters of the optical counterpart candidate of J1944 from the *Gaia* catalog. The distance D corresponds to the geometric distance according to *Gaia* (Bailer-Jones, et al., 2021).

R.A. (J2000)	19 ^h 44 ^m 01 ^s 898273(4)
Dec. (J2000)	+28°44′51″58412(6)
Gal. longitude l , deg.	64.226
Gal. latitude b , deg.	2.396
Parallax π , mas	2.405(75)
Proper motion μ , mas yr ⁻¹	35.766
μ_{ra} , mas yr ⁻¹	32.56(6)
μ_{dec} , mas yr ⁻¹	14.81(7)
Distance D , pc	415(15)

with the pixel scale 0.33'' and binning 1×1.

The object was also observed with the 2.1-m OAN-SPM telescope using the “Rueda Italiana” instrument¹ in the V band on June 1, 2023. The field of view of the detector is 6′×6′ with a pixel scale of 0.34'' and binning 2×2.

Photometric data were reduced using the IRAF package². The direct images were bias subtracted and flat-field corrected. Cosmic rays were removed using the LaCosmic (van Dokkum, 2001) algorithm. Source detection in images was performed using the DAOFIND algorithm. Since wings from the nearest star are superimposed on the profile of the J1944 candidate, the PSF photometry was used to correctly calculate the fluxes.

We also carried out fast photometry with the 6-m BTA telescope of the Special Astrophysical Observatory of the Russian Academy of Sciences in 2022. These observations used the MANIA complex based on a multimode panoramic photopolarimeter (MPPP) with microsecond time resolution (Plokhotnichenko, et al., 2021, 2023). The instrument was installed at the Nasmyth1 BTA focus, equipped with a rotary table that compensated the field of view rotation with a diameter of about 20''. The emission of this sky region in the range 3600 – 7600 Å, divided at a wavelength of 4500 Å into two beams by a dichroic mirror, was synchronously recorded by coordinate-sensitive detectors (CSD) with

¹<https://www.astrossp.unam.mx/en/users/instruments/ccd-imaging/filter-wheel-italiana>

²The IRAF astronomical data processing and analysis package is available at <https://iraf-community.github.io>

a sensitivity maximum in the red and blue parts of the spectrum (Debur, et al., 2003; Plokhotnichenko, et al., 2009). The coordinates and arrival times of photons were detected and encoded by the multidimensional chronometric device “Kvantokhron 4-48” (Plokhotnichenko, et al., 2009) with a time resolution of 1 μ s and stored as a data array in the computer memory. The data arrays were converted into photon lists containing sequences of arrival times and coordinates of the detected photons. Using the photon lists, the dynamic images of the MPPP field of view and the light curves of selected sources (the object, a reference star, and two check stars) were constructed, and the statistical parameters were determined. At the same time, the effects of the atmospheric instability, variations in the telescope guiding speed, as well as the uneven movement of the rotary table were compensated.

The log of all observations is presented in Table 2.

Optical spectroscopy

Spectral data of the presumed optical counterpart of J1944 were obtained with the 6-m BTA telescope of the Special Astrophysical Observatory of the Russian Academy of Sciences on July 4/5 and July 7/8, 2022 in the director’s reserve quota. The observations were carried out under good astroclimatic conditions with a seeing of 1.2 – 1.3''. The spectra were obtained using the SCORPIO-2 focal reducer in the long-slit spectroscopy mode (Afanasiev, Moiseev, 2011). The VPHG1200@540 volume phase holographic grating with a 1'' slit width were used, providing the spectral resolution $\delta\lambda \approx 5.5$ Å in the $\lambda\lambda = 3650 - 7250$ Å range. The spectra were reduced using the IRAF package. Spectral images were bias subtracted, cleared of cosmic rays using the LaCosmic program, and corrected for inhomogeneous sensitivity by flat-field division. Using He-Ne-Ar lamp images, the spectra were wavelength calibrated and corrected for geometric distortions. Optimal extraction of spectra with subtraction of the sky background (Horne, 1986) was performed. The source spectra were flux calibrated using the spectra of the standard star BD+25°4655 (Oke, 1990). We also calculated heliocentric radial velocity corrections for each spectrum. The log of spectral observations is included in Table 2.

Таблица 2. Observation log of the J1944 optical counterpart candidate. The telescopes and instruments used in the observations, date and duration, number of images obtained (N), exposure time, and spectral range are presented.

Telescope/Instrument	Date (UT)	Duration HJD–2459700	N	Exposure sec	Spectral range
RTT-150/TFOSC	13/14-05-2022	13.4848–13.5940	62	120	<i>g, r, i</i>
RTT-150/TFOSC	15/16-05-2022	15.4831–15.5865	44	180	<i>r</i>
RTT-150/TFOSC	01/02-06-2022	32.4337–32.5634	63	180	<i>i</i>
BTA/SCORPIO-2	04/05-07-2022	65.3705–65.4836	28	300	3650–7250 Å
BTA/SCORPIO-2	07/08-07-2022	68.4214–68.4892	17	300	3650–7250 Å
BTA/MANIA	06/07-07-2022	67.3822–67.4100	3230	1	3600–7600 Å
BTA/MANIA	06/07-07-2022	67.4197–67.5000	7999	1	3600–7600 Å
2.1-m/Rueda Italiana	01/02-06-2023	396.8990–396.9669	51	100	<i>V</i>
RTT-150/TFOSC	15/16-06-2023	411.4484–411.5523	20	120	<i>r</i>
RTT-150/TFOSC	11/12-07-2023	437.4336–437.5480	90	60	<i>g</i>
RTT-150/TFOSC	12/13-07-2023	438.4625–438.5642	76	120	<i>r</i>
RTT-150/TFOSC	15/16-07-2023	441.4186–441.5569	80	120	<i>r</i>
RTT-150/TFOSC	07/08-06-2024	769.4924–769.5603	70	60	<i>g</i>
RTT-150/TFOSC	09/10-06-2024	771.4218–771.5535	140	60	<i>g</i>
RTT-150/TFOSC	15/16-06-2024	777.4203–777.4512	12	180	<i>g, r, i, z</i>

Archival UV observations

The J1944 field was observed with the *Swift* telescope in 2018 and 2022 – 2024. We analyzed Ultra-violet/Optical Telescope (UVOT) data obtained in the *uvw2* (1928 Å), *uvm2* (2246 Å), *uvw1* (2600 Å) and *u* (3465 Å) bands using processed images from the archive. For photometry we used the UVOTSOURCE command and a standard aperture of 5". The list of observations and photometry results are presented in Table 3. The J1944 flux in the *u* band is contaminated by the light from nearby stars (Fig. 2), while this is negligible at shorter wavelengths. Observations 03111808002 and 00010695019 were excluded from consideration because they had UVOT exposures of 7 and 0 sec, respectively.

X-ray data

The J1944 field was observed with the eROSITA telescope with the total exposure time of 669 sec. To extract the source spectrum, we used a circle with a radius of 60", and the background spectrum was extracted from an annulus with radii of 120" and 300".

J1944 was also monitored with the X-Ray Telescope (XRT) on board the *Swift* observatory. Observations analyzed in this work are listed in Table 3 with addition of ObsIDs 03111808002 and 00010695019. *Swift*-XRT data products generator

tools³ (Evans, et al., 2009), were used to obtain the light curve and to extract spectra of the source.

DATA ANALYSIS AND RESULTS

Optical and UV images

Images of the J1944 field obtained by the RTT-150 telescope in the *r* band and *Swift*/UVOT in the *uvw1* band are shown in Fig. 2. As can be seen, in 2022 the source was brighter than in 2023, both in the optical and UV, which indicates its strong variability. Fig. 3 shows an image of the J1944 vicinity detected by the red CSD with an exposure of 8000 sec on July 6/7, 2022.

Variability on long time scales

To consider the optical and UV variability of the counterpart candidate of J1944 and the source itself in X-rays, we collected available archival data covering the period from 2005 to 2024. The light curves compiled from ZTF, Pan-STARRS, IPHAS, *Swift* UVOT and XRT data are shown in Fig. 4. As seen from the figure, in the optical and UV, the source exhibits strong variability on time scales from hours to months and years. The high and low states are clearly resolved with average magnitudes of $\sim 18^m$ and $\sim 20^m$, respectively. Transitions from the low to the high state occurred around MJD 55800 and 60300 and from the high to the low state

³https://www.swift.ac.uk/user_objects/

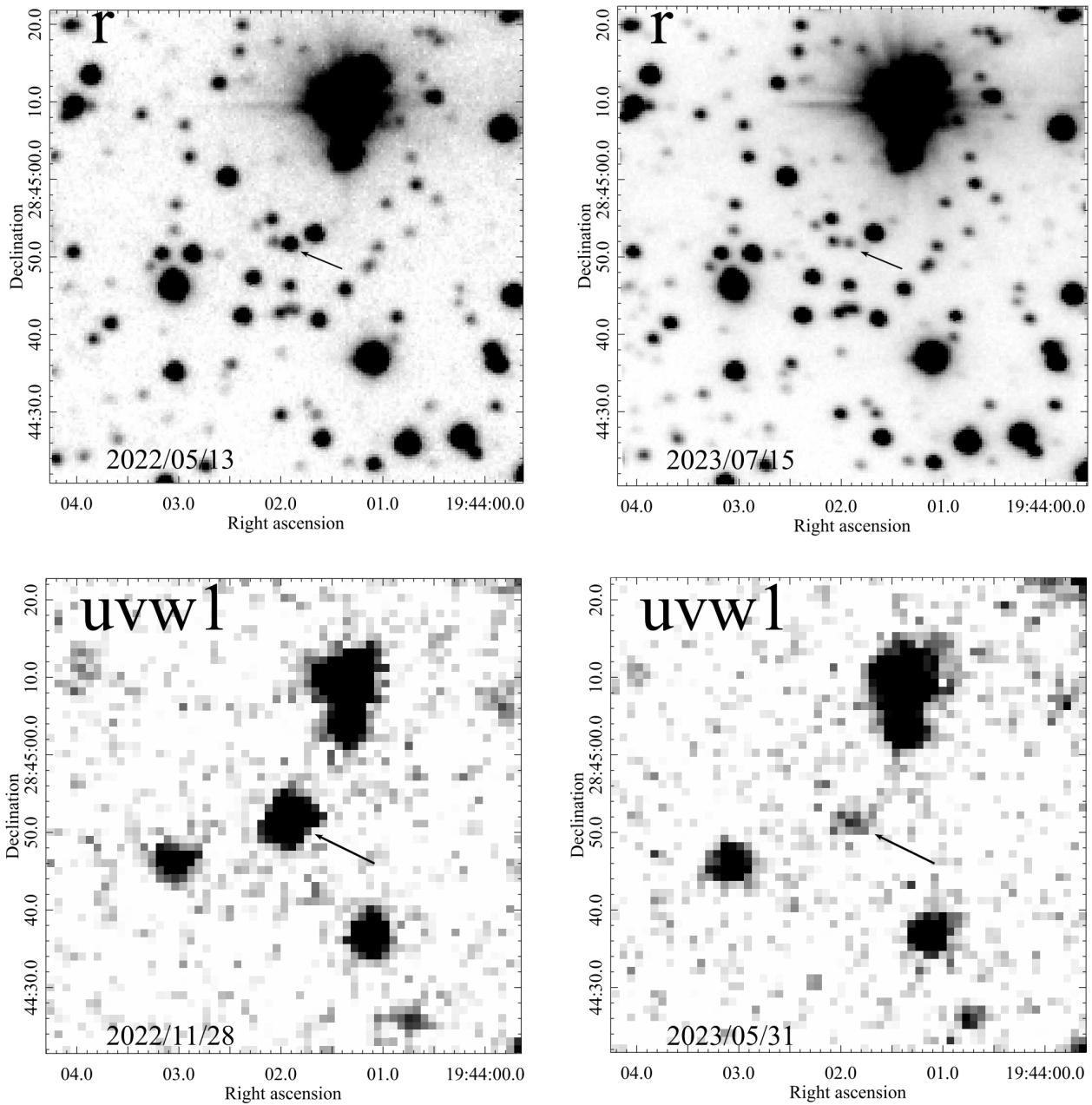


Fig. 2. $1' \times 1'$ images of the J1944 field obtained by the RTT-150 in the *r* band (top) and *Swift*/UVOT in the *uvw1* band (bottom). The arrow marks the J1944 position. The left and right panels show the high and low state of the source, respectively.

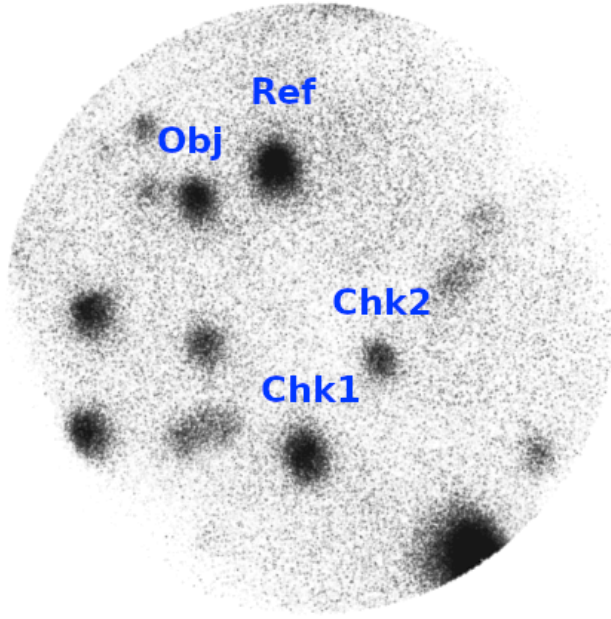


Fig. 3. Image of the J1944 field with a diameter of $20''$ obtained with the MPPP multimode photopolarimeter. The source J1944 is labeled as “Obj”, the reference star is “Ref”, and the two check stars are “Chk1” and “Chk2”.

around MJD 60000 and 60447. In the high state, the variability amplitude is about two magnitudes, and in the low state it is significantly smaller.

In X-rays, J1944 also shows transitions between the high and low states, consistent in time with the transitions in the optical/UV. This proves that the optical source is indeed the counterpart of J1944.

Such variability is typical for tight binary systems with accreting compact objects, such as CVs (Honeycutt, Kafka, 2004; Mason, Santana, 2015; Mukai, Pretorius, 2023), transitional millisecond pulsars (tMSPs, Papitto, de Martino 2022), or low-mass X-ray binaries (Mitsuda, et al., 1989).

Optical variability on short time scales

Light curves of the J1944 optical counterpart in the high state, obtained with the RTT-150 telescope, are shown in Fig. 5. On May 13/14 2022, we carried out multiband photometric observations in the g , r and i filters of the SDSS system. All bands exhibit quasi-simultaneous brightness variations with an amplitude of $\Delta g \approx \Delta r \approx \Delta i \approx 0.5^m$ on a time scale of ~ 1 hour. Changes in brightness between individual exposures are also noticeable, significantly exceeding photometric errors $\delta m = 0.02 - 0.05^m$.

On May 15/16 we observed quasi-periodic brightness changes with an amplitude of $\Delta r \approx 0.4^m$

and a variability time of 86 minutes (Fig. 5). In the observations of June 01/02 2022, no periodicity appears. The brightness of the system gradually decreased by $\Delta i \approx 0.4^m$ over ≈ 0.12 day, but then abruptly increased to the initial value in ≈ 0.01 day.

The J1944 light curves in the low state, obtained with the OAN-SPM and RTT-150 telescopes in 2023, are presented in Fig. 6 on the left. The source does not show such strong variations as in the high state. Having performed periodogram analysis using the Lomb-Scargle method, we found a period P_s equal to 7.96 ± 0.07 min (central panels in Fig. 6). The light curves folded with this period show one peak per period with a brightness variation of no more than 0.4^m (Fig. 6 on the right). To check the stability of this periodicity, additional photometric data were obtained with the RTT-150 in the g filter on 07/08 and 09/10 June 2024 when the source was again in the low state. Analysis of the light curves using the Lomb-Scargle method resulted in a period of 7.948 ± 0.011 min with an amplitude of 0.4^m , which confirms the high stability of the period and amplitude of the periodic brightness variations in the low state over one year.

Based on the results of data processing from the MANIA complex (Fig. 3), obtained on July 6/7, 2022 at the 6-m BTA telescope when the source was in the high state, we constructed light curves of J1944 and field stars with a time resolution of 1, 5 and 10 sec. Fig. 7 shows the light curves with a time window of 10 sec as the difference between the instrumental magnitudes of the object and the reference star (Ref) (blue line), as well as the check star (Chk2) and Ref (orange line). The identical long-term (over hours) brightness variations are due to the effect of field vignetting and imperfect field rotation correction. As a result of reduction, light curves with a resolution of 1 min were obtained in the relative magnitudes Obj – Ref and Chk1 – Ref, shown in Fig. 8. Based on the analysis of the results, we came to the following conclusions:

- no significant variability was detected on time scales of $\sim 1 - 10$ sec. Taking into account statistical and systematic errors, the limit on the amplitude of such variability is $\sim 0.25^m$.
- stochastic variations were detected on time scales of 1 – 15 min and observed in light curves with amplitudes of $0.2 - 0.6^m$.

Apparently, this behavior is caused by large-scale turbulence of the accretion structure around the compact object.

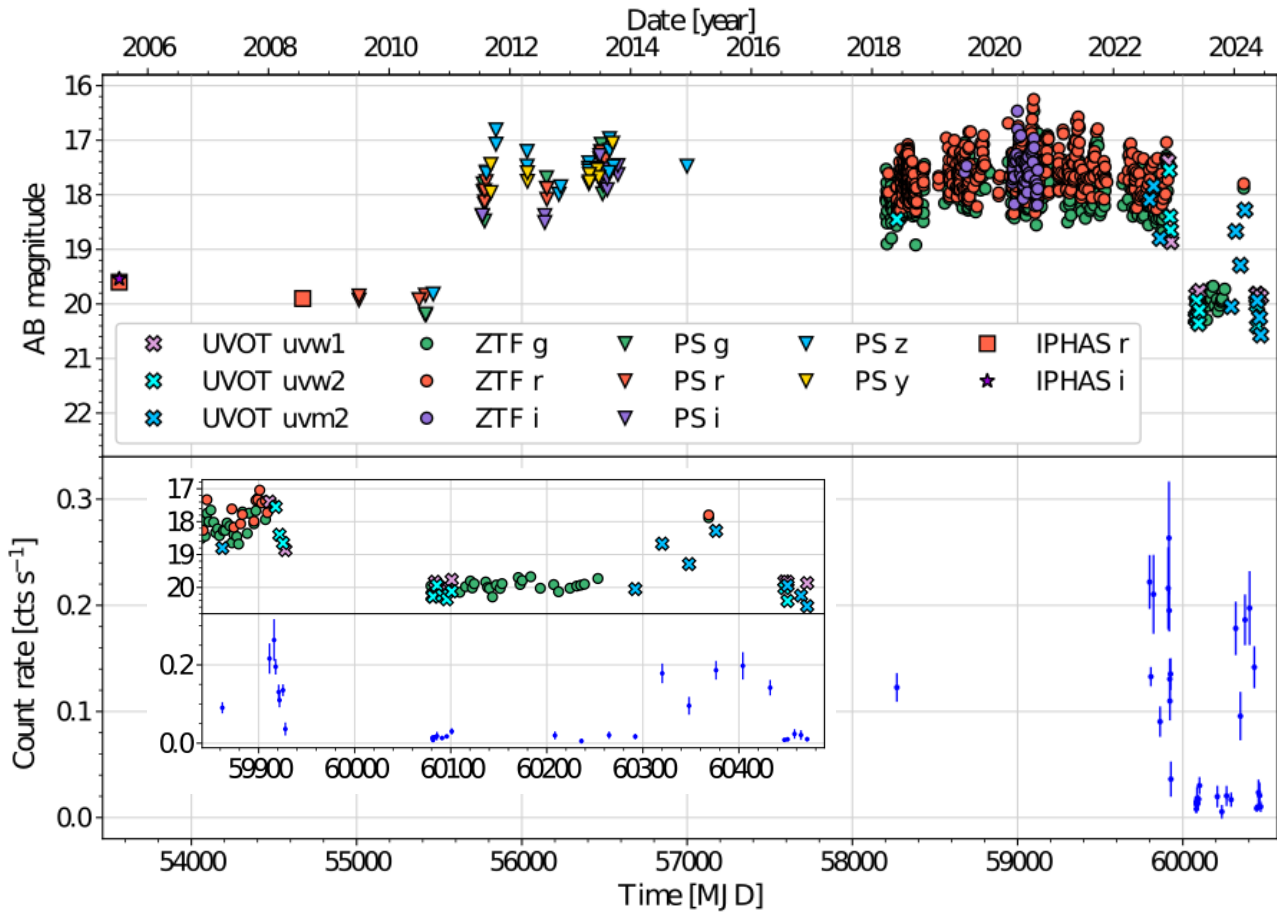


Fig. 4. Top: Optical light curves of J1944 based on the data obtained from various catalogs and instruments in the optical and UV filters notified in the legend (PS \equiv Pan-STARRS). Bottom: X-ray light curve of J1944 obtained with the *Swift*/XRT telescope in the 0.3 – 10 keV range. The recent time interval is zoomed in and shown in the insert.

Таблица 3. List of *Swift*/UVOT observations of J1944 and photometry results (given in the AB system). Uncertainties do not take into account the systematic error of 0.03^m .

ObsID	Date	<i>uvw1</i>	<i>uvw2</i>	<i>uvm2</i>	<i>u</i>
00010695002	31-05-2018		18.45±0.04		
03111808001	07-08-2022			18.09±0.05	
03111808003	31-08-2022			17.84±0.07	
03111808004	10-10-2022			18.80±0.07	
03111808005	28-11-2022	17.39±0.05			
03111808006	03-12-2022				16.62±0.04
03111808007	04-12-2022		17.55±0.05		
03111808008	07-12-2022				17.47±0.05
03111808009	08-12-2022		18.40±0.05		
03111808010	12-12-2022		18.65±0.06		
03111808011	14-12-2022	18.86±0.11			
00010695003	17-05-2023		20.27±0.10		
00010695004	17-05-2023		20.23±0.10		
00010695005	17-05-2023		20.28±0.10		
00010695007	19-05-2023	19.83±0.19			
00010695008	21-05-2023		19.94±0.14		
00010695009	26-05-2023	20.05±0.24	20.24±0.18		18.98±0.17
00010695010	31-05-2023	20.11±0.22	20.36±0.15		18.85±0.14
00010695011	06-06-2023	19.77±0.17	20.12±0.12		
00010695012	21-09-2023				19.12±0.12
00010695013	19-10-2023				19.18±0.13
00010695014	16-11-2023				18.97±0.09
00010695015	14-12-2023			20.05±0.18	
00010695016	11-01-2024			18.67±0.08	
00010695017	08-02-2024			19.29±0.13	
00010695018	07-03-2024			18.28±0.06	
00010695020	02-05-2024				17.33±0.03
00010695022	17-05-2024	19.82±0.26	20.02±0.26		18.79±0.13
00010695023	20-05-2024	19.83±0.15	20.41±0.20	19.94±0.17	18.80±0.09
00010695025	27-05-2024		20.25±0.19		
00010695026	03-06-2024				18.58±0.11
00010695027	09-06-2024	19.87±0.22	20.57±0.20		

Optical spectra

Averaged optical spectrum of J1944 in the high state is shown in Fig. 9. It reveals a blue continuum, double-peaked hydrogen emission lines of the Balmer series ($H\alpha$, $H\beta$, $H\gamma$, $H\delta$, $H\epsilon$, $H\zeta$), neutral helium (HeI $\lambda 4023$, $\lambda 4387$, $\lambda 4471$, $\lambda 4713$, $\lambda 4921$, $\lambda 5015$, $\lambda 5876$, $\lambda 6678$, $\lambda 7065$), the lines of ionized helium HeII $\lambda 4686$ and iron FeII $\lambda 5169$. This is typical for spectra of accretion disks in close binary systems.

The dynamic spectrum of the HeI $\lambda 5876$ line, obtained from the observations on July 04/05, 2022, is shown in the left panel of Fig. 10. It exhibits a weak S-wave, which is often presented in spectra of CVs with accretion disks. The footprints of this wave also appear in the other lines profiles, but it is most obvious in the HeI $\lambda 5876$ line. Probably, it forms in a hot spot when the accretion flow interacts with the outer edge of the accretion disk. To separate the S-wave, we subtracted the averaged profile from the line profiles. The dynamic spectrum of HeI $\lambda 5876$ obtained from the residual profiles is shown in the right panel of Fig. 10. Fitting the S-wave with a sinusoid, we estimated the radial velocity semi-amplitude of the hot spot $K_s = 650 \pm 23 \text{ km s}^{-1}$ and the period $P = 89 \pm 1 \text{ min}$. Since the radial velocities of the hot spot are modulated by the orbital motion, the period can be considered as the orbital one.

To estimate the parameters of the system, the semi-amplitude of the radial velocity curve of the accretor K_1 is required. Although there is no evidence of an accretor in the spectra of J1944, its orbital motion is reflected by emission lines formed in the accretion disk. An accurate calculation of K_1 requires measuring radial velocities from the wings of spectral lines. The wings form closer to the accretor and are less distorted by hot spot radiation and tidal deformations of the accretion disk. To solve this problem, we used the method proposed by Shafter (1983). It consists of a convolution of the form

$$C(v_0) = \int k(v - v_0)r(v)dv, \quad (1)$$

where $r(v)$ is the spectral line profile in the velocity scale, and the kernel k is the difference of two Gaussians separated by a distance a , i.e.

$$k(v) = \exp\left[-\frac{(v + a/2)^2}{2\sigma^2}\right] - \exp\left[-\frac{(v - a/2)^2}{2\sigma^2}\right]. \quad (2)$$

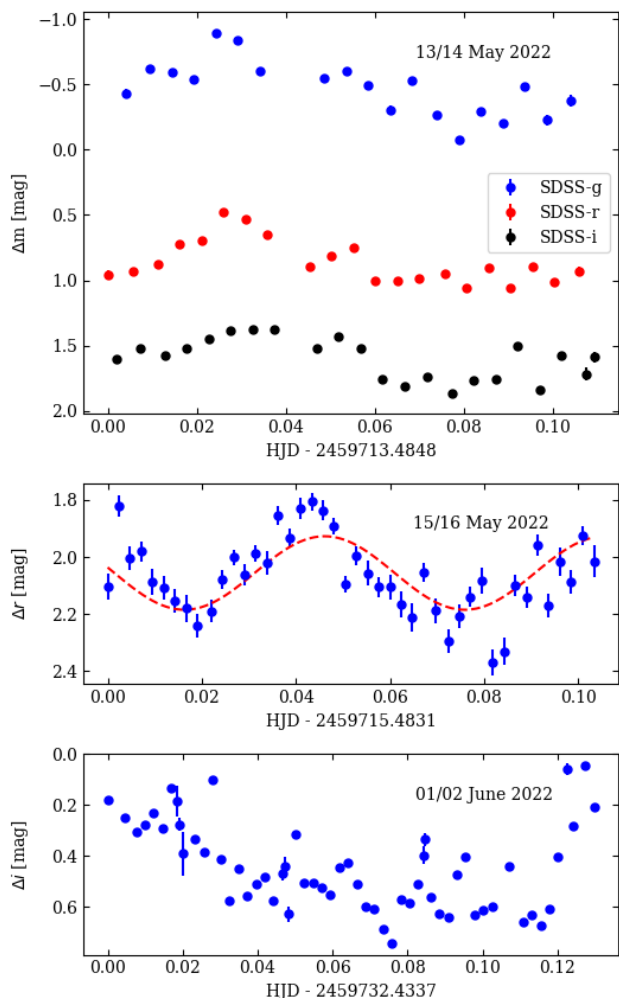


Fig. 5. Light curves of the optical companion candidate of J1944, obtained with the RTT-150 on May 13/14, May 15/16, June 01/02, 2022. The light curve of May 15/16 is approximated by a sinusoid with a 86 min period.

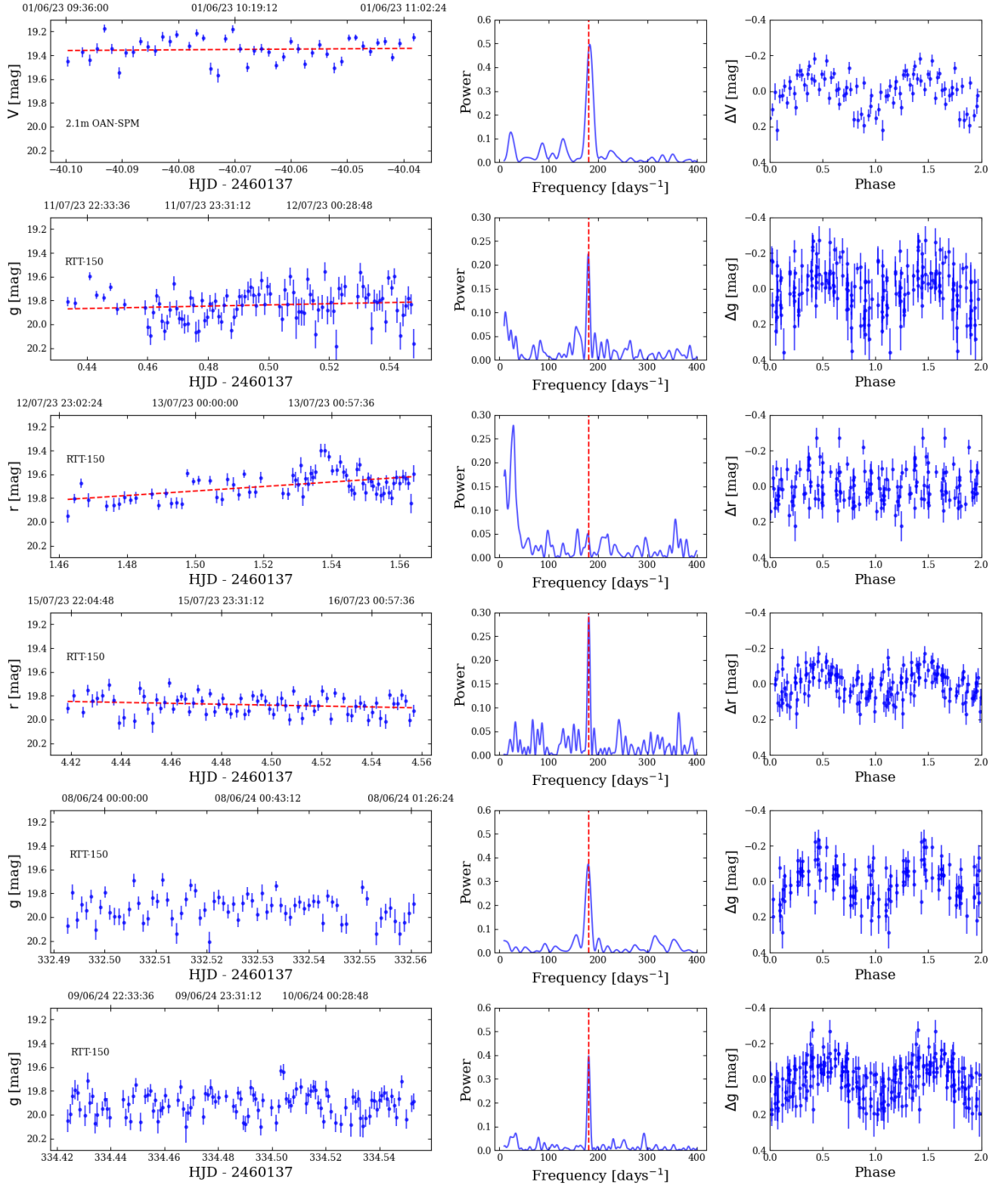


Fig. 6. Light curves of J1944 in the low state (left), Lomb-Scargle periodograms (middle) and light curves folded with the period $P_s = 7.96 \pm 0.07$ min ($f_s = 181.00 \pm 1.66$ day $^{-1}$) obtained from the periodograms (right). In the left plots, the dotted line shows the trend subtracted before calculating the periodograms. Data points of the OAN-SPM telescope are given in the Vega system.

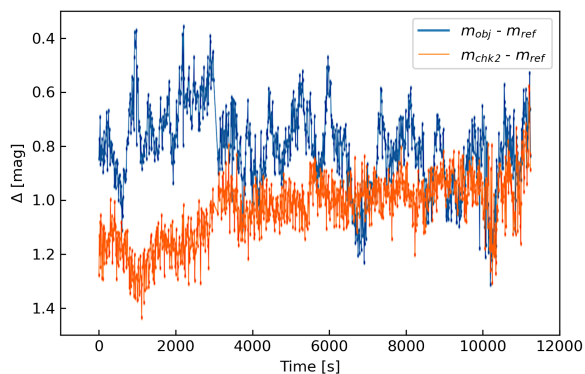


Fig. 7. 10-sec time resolution light curves obtained with the MPPP instrument for J1944 (blue line) and the check star (orange line).

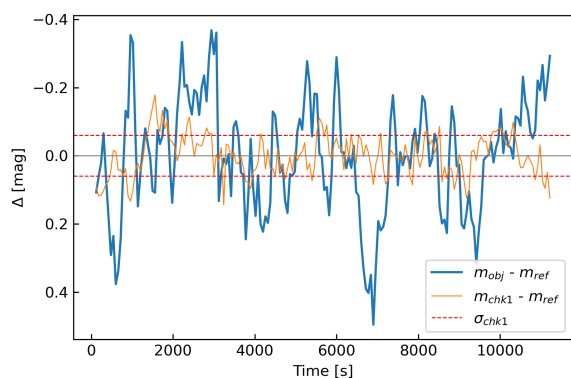


Fig. 8. Light curves of J1944 and the reference star with 60-sec time resolution, obtained from observations with the multimode photopolarimeter MPPP. The red dashed lines show the 1σ uncertainty calculated from the reference star.

a is selected to provide the locations of Gaussians in the line wings. The standard deviations σ must be small enough that the Gaussians do not take into account the central parts of the line. On the other hand, Gaussians must be wide enough to collect sufficient signal. The radial velocity of the line wings v_0 is determined from the requirement $C(v_0) = 0$. The resulting radial velocity curves were approximated by sinusoids $v_0(t) = \gamma - K_1 \sin[2\pi(t/P_{orb} - \varphi_0)]$, where γ is the average radial velocity, K_1 – the radial velocity semi-amplitude of accretor ($K_1 > 0$) and φ_0 – the initial phase. To select the separation of the Gaussians a , we used diagnostic diagrams representing the dependences of the semi-amplitude K and its error ΔK on the separation a . To select the optimal separation of the Gaussians a , we used diagnostic diagrams representing the dependences of the semi-amplitude K and the error ΔK on the distance a . We select the distance $a = 2500$ km/s as the maximum value, after that the error ΔK increases rapidly. The standard deviation is assumed to be $\sigma = 150$ km s $^{-1}$. The resulting radial velocity curves for the lines H α , H β , H γ , HeI $\lambda 5876$ (with the average velocity γ subtracted) are shown in Fig. 11. The radial velocity mean errors are ≈ 5 km s $^{-1}$ for the H α line, ≈ 9 km s $^{-1}$ for the H β line, ≈ 16 km s $^{-1}$ for the lines H γ and HeI $\lambda 5876$. This corresponds to the previously found orbital period. The radial velocity semi-amplitude estimate is $K_1 = 30 \pm 5$ km s $^{-1}$, and the derived mass function is $f_2(M) = 0.00017(9)M_\odot$.

Doppler tomograms were reconstructed from the profiles of the H α and HeI $\lambda 5876$ lines and are shown in Fig. 12. They represent the velocity distribution of emission line sources projected onto the orbital plane. The points in this space have two coordinates: the velocity module v , measured from the center of mass, and the angle ϑ between the velocity vector and the line connecting the centers of mass of the stars in the system. For a more detailed introduction to the Doppler tomography method, we refer to Marsh, Schwope (2016); Kotze, et al. (2015); Kotze, Potter, et al. (2016). The reconstruction of Doppler maps was carried out using the code doptomog-2.0 (Kotze, et al., 2015) with the maximum entropy method. The orbital phases of the spectral exposure midpoints were calculated from the radial velocity curves of the accretor. Due to the zero phase error φ_0 , the Doppler tomograms have an uncertainty in the rotation angle of $\Delta\theta = 6^\circ$ and $\Delta\theta = 9^\circ$ in the observations of 04/05 July and 07/08 July 2022, respectively. In all tomograms presented in Fig. 12,

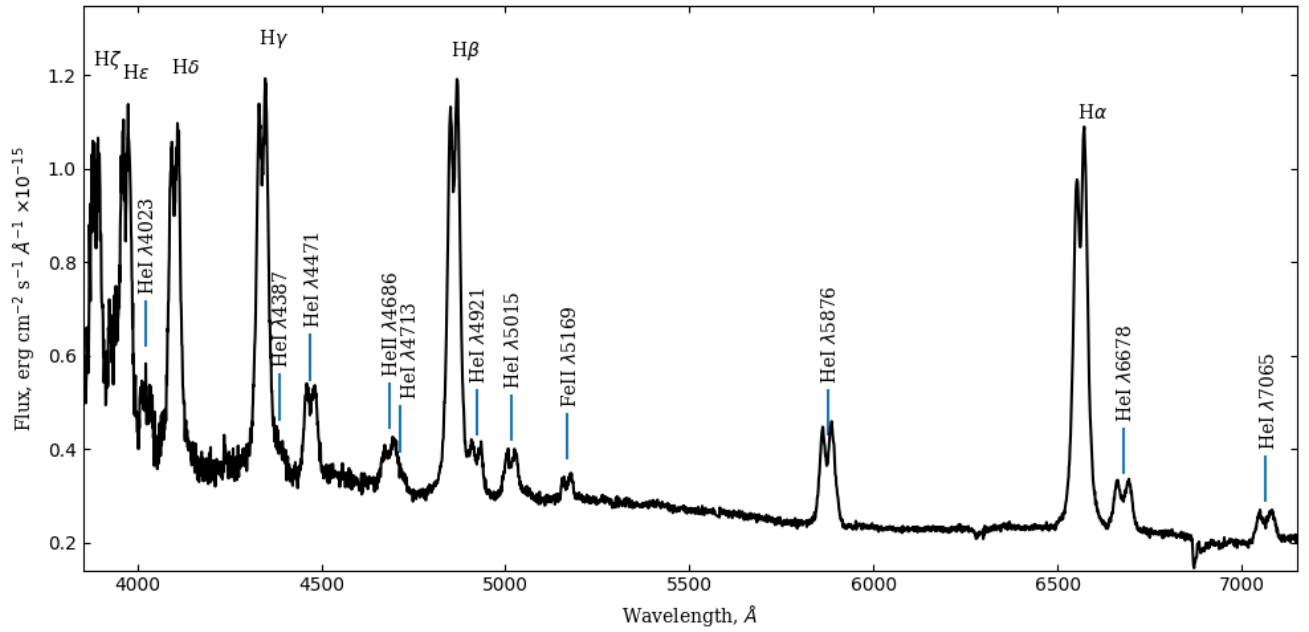


Fig. 9. Averaged optical spectrum of the J1944 counterpart candidate.

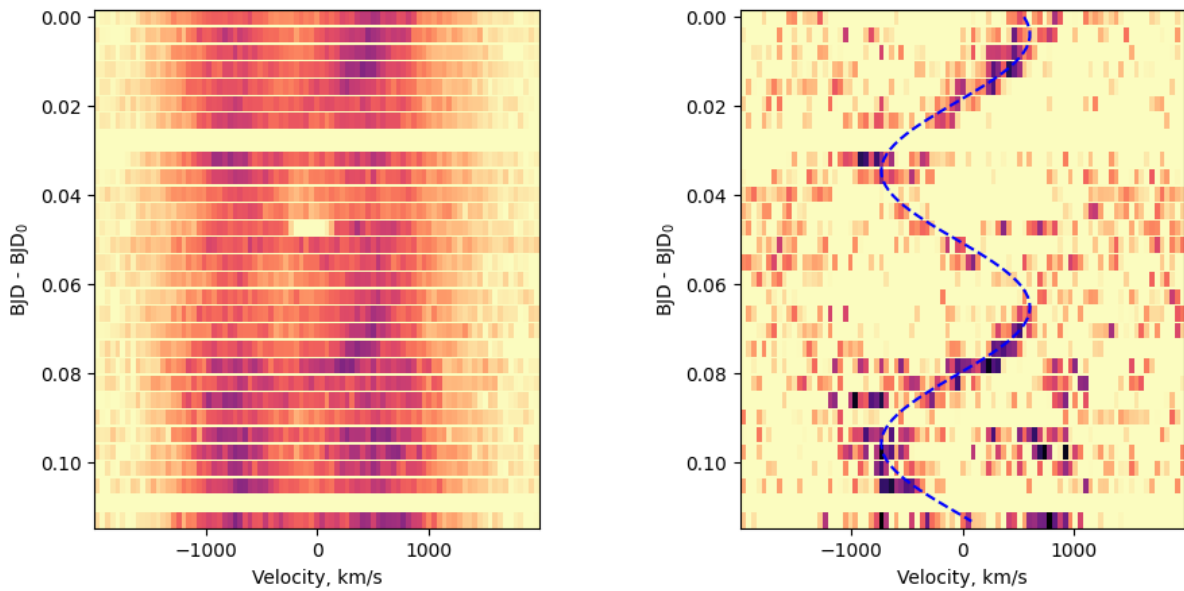


Fig. 10. Dynamic spectrum of the HeI $\lambda 5876$ line (left) and the residual spectrum after subtracting the average line profile (right). The initial epoch BJD_0 corresponds to the middle of the exposure of the first spectrum.

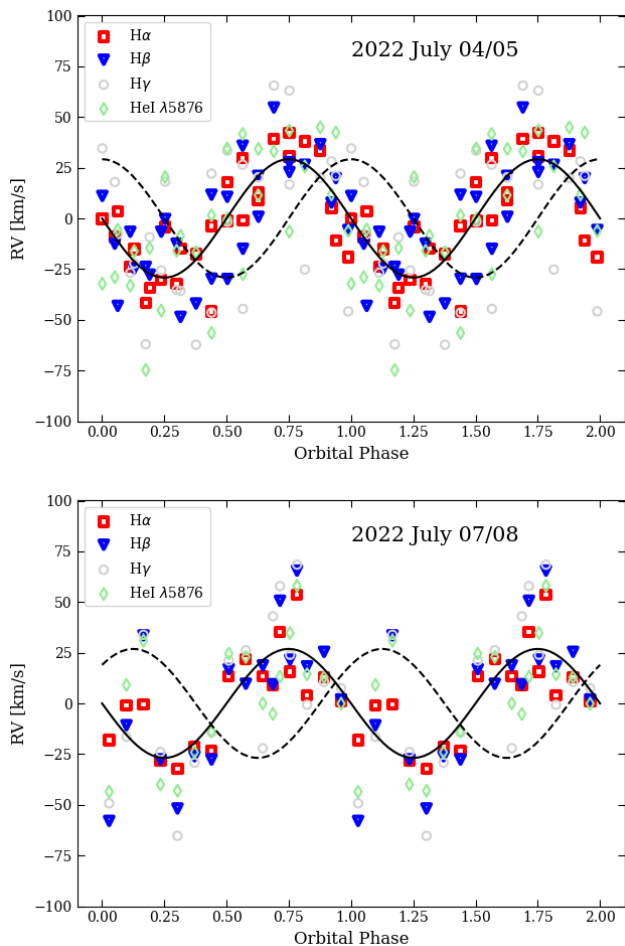


Fig. 11. Radial velocity curves of the $H\alpha$, $H\beta$, $H\gamma$ and $\text{HeI } \lambda 5876$ lines wings, obtained from the observational data on July 04/05, 2022 (top panel) and July 07/08 2022 (bottom panel). The black line shows the approximating sinusoid. The dotted line corresponds to the radial velocity curve of the hot spot divided by K_s/K_1 .

Таблица 4. Results of the fitting of the J1944 X-ray spectra with the TBABS \times (MEKAL+MEKAL) model. Uncertainties are at the 1σ confidence level. The superscripts h and l correspond to the J1944 high and low states. VEM is a volume emission measure. $D_{415} \equiv D/(415 \text{ pc})$.

$N_{\text{H}}, \text{cm}^{-2}$	$5.8^{+1.3}_{-1.4} \times 10^{20}$
T_1, keV	$0.61^{+0.07}_{-0.09}$
$\text{VEM}_1^h, \text{cm}^{-3}$	$(4.1 \pm 0.9) \times 10^{53} D_{415}^2$
$\text{VEM}_1^l, \text{cm}^{-3}$	$1.5^{+0.4}_{-0.3} \times 10^{53} D_{415}^2$
T_2, keV	$5.94^{+1.26}_{-0.74}$
$\text{VEM}_2^h, \text{cm}^{-3}$	$6.1^{+0.3}_{-0.2} \times 10^{54} D_{415}^2$
$\text{VEM}_2^l, \text{cm}^{-3}$	$3.7^{+0.6}_{-0.7} \times 10^{53} D_{415}^2$
$F_X^h, \text{erg s}^{-1} \text{cm}^{-2}$	$5.72^{+0.28}_{-0.24} \times 10^{-12}$
$F_X^l, \text{erg s}^{-1} \text{cm}^{-2}$	$4.53^{+0.50}_{-0.46} \times 10^{-13}$
$L_X^h, \text{erg s}^{-1}$	$1.18^{+0.06}_{-0.05} \times 10^{32} D_{415}^2$
$L_X^l, \text{erg s}^{-1}$	$9.33^{+1.04}_{-0.94} \times 10^{30} D_{415}^2$
χ^2/ν	88.9/79
C/ν	26.8/20

there is a ring-shaped structure that corresponds to the accretion disk. The tomograms also show a hot spot formed as a result of the accretion flow interaction with the outer edge of the accretion disk. The position of the hot spot on tomograms in the $\text{HeI } \lambda 5876$ line obtained in two various nights differs by $\theta \sim 15^\circ$ and can be explained by initial epoch errors in orbital ephemeris. The position of the hot spot on tomograms in the $H\alpha$ line shifts significantly in $\Delta\theta \approx 45^\circ$ and probably reflects a change in the location of the emission source. From a comparison of tomograms in the two lines, it is obvious that $\text{HeI } \lambda 5876$ emissions are formed in higher-velocity regions of the disk that are closer to the accretor.

X-ray spectra

Observations with the SRG/eROSITA were performed during the high state of J1944. 872 counts from the source (excluding background) were detected in the 0.3 – 9 keV range and they were regrouped to have at least 20 counts per energy bin.

In the case of the *Swift*/XRT data, we extracted two spectra. The first one includes the data obtained on 2018, 2022 and 2024 (up to May 17) in the high state of J1944. The second one includes the data obtained on 2023 and 2024 (from May 17) in the low state of J1944. For the high state spectrum, the effective exposure was about 8.7 ks, and 965 counts were collected from the source in

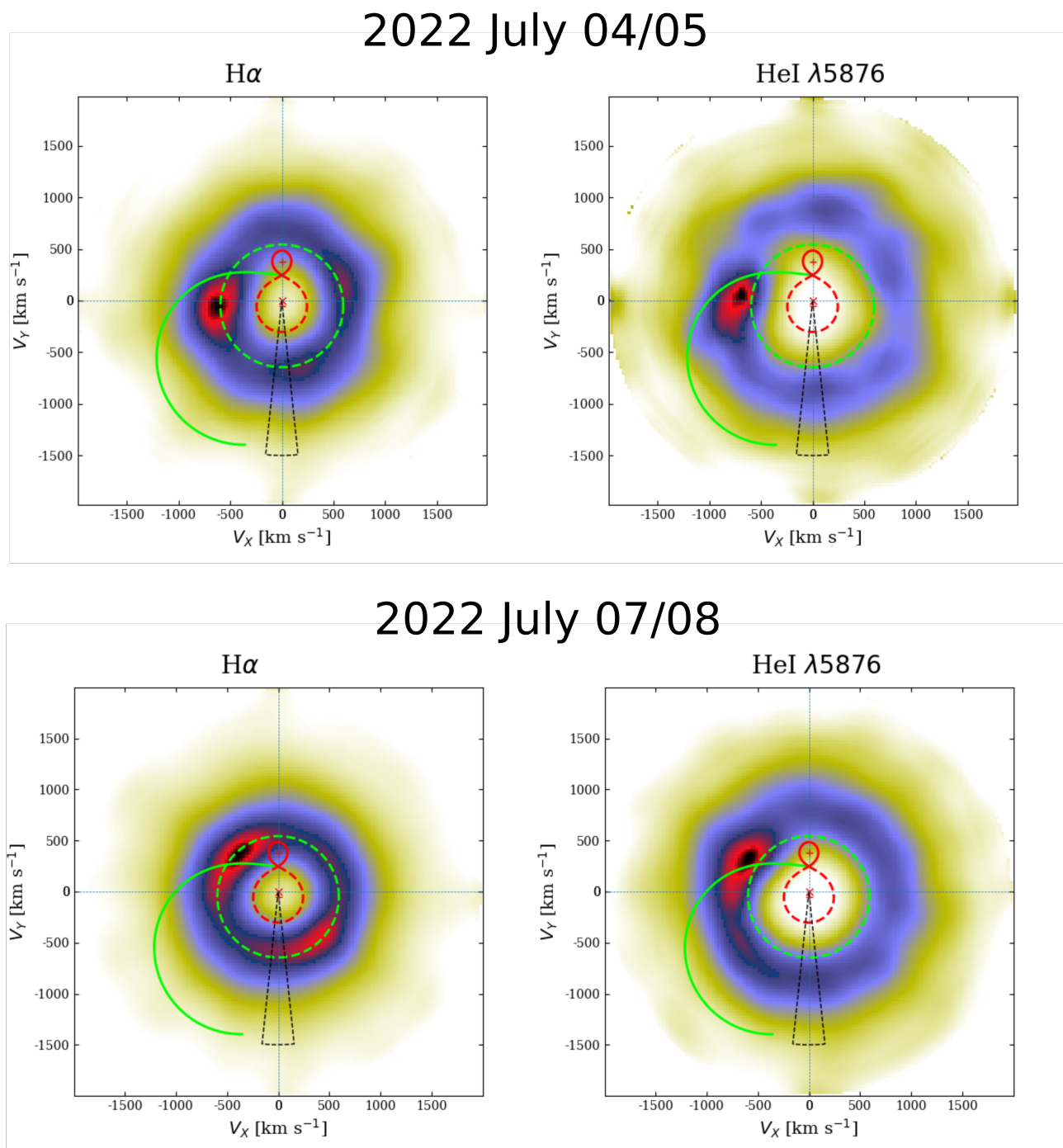


Fig. 12. Doppler tomograms of J1944 in the $H\alpha$ (left) and $HeI \lambda 5876$ (right) emission lines. The tomograms were reconstructed from the observational data on July 04/05, 2022 (top) and July 07/08, 2022 (bottom). The tomograms show the velocities of the Roche lobe of the primary (dotted red line) and secondary components (solid red line). There are also plotted the ballistic trajectory (solid green line) originating from the Lagrange point L_1 and the particle velocities at the outer edge of the accretion disk (dashed green line) corresponding to the 3 : 1 resonance. The angle of the dotted sector corresponds to the tomogram rotation uncertainty associated with the zero epoch error of the orbital ephemeris. The binary system model is calculated for the accretor mass $0.6 M_{\odot}$, mass ratio $q = 0.13$ and the inclination $i = 65^{\circ}$ (see “Discussion” section).

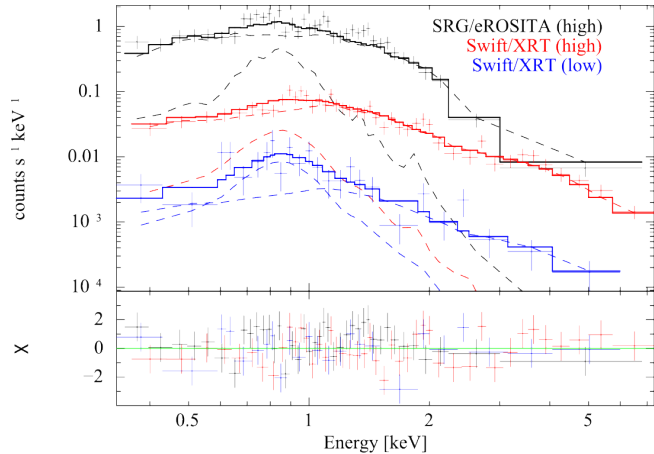


Fig. 13. J1944 X-ray spectra in the high and low states obtained from the *Swift*/XRT and SRG/eROSITA data. The best-fitting 2-T MEKAL model (thick solid lines) and its components (dashed lines) are shown. Fit residuals are presented in the bottom sub-panel.

the 0.3 – 10 keV range. We regrouped it to have at least 20 counts per energy bin. For the low state spectrum, the effective exposure was 14.1 ks, but only 130 counts were detected. We regrouped it to obtain at least 5 counts per energy bin.

Spectra extracted from the *Swift* and eROSITA data were fitted in the 0.3 – 10 keV range using the XSPEC software package (Arnaud, 1996). We used the χ^2 statistic for the high state data and the C -statistic (Cash, 1979) for the low state data due to the small number of counts.

We fitted the spectra with the MEKAL thermal plasma model (Mewe, et al., 1985, 1986; Liedahl, et al., 1995). Similar models are used to describe the X-ray spectra of CVs (see, for example, Baskill, et al., 2005; Reis, et al., 2013; Nucita, et al., 2014). At the initial analysis step, the temperature and normalization of the model were considered as free parameters for each spectrum, to evaluate possible variations of source parameters over time. To take into account the interstellar absorption, the TBABS model with the WILM elemental abundances (Wilms, et al., 2000) was used. The equivalent absorbing hydrogen column density N_{H} for all spectra was linked.

For the high-state eROSITA and *Swift* spectra, the reduced χ^2 are $\chi^2_{\nu} = 1.4$ (degrees of freedom $\nu = 37$) and 1.2 ($\nu = 41$), and for the *Swift* low-state spectrum, $C_{\nu} = 2.1$ ($\nu = 22$). The fits show some excesses of the observed flux compared to the model at energies $\lesssim 1$ keV.

Then we used the two-temperature model 2-T

MEKAL. In this case, the fits are acceptable. For all the three spectra, the derived temperatures T_1 and T_2 are consistent within 2σ uncertainties. For the two high state spectra, the normalizations of the thermal components are consistent, while for the low state data the normalization is lower, as expected from the light curve (Fig. 4, bottom). The parameters for the latter case are determined poorly due to the small number of counts. Finally, we fitted the three spectra simultaneously, assuming that all parameters are common except for normalizations of model components. The results of the fit, the unabsorbed fluxes F_X^h and F_X^l in the high and low states in the 0.3 – 10 keV range, as well as the luminosities L_X^h and L_X^l are presented in Table 4. The spectra and the best-fitting model are shown in Fig. 13.

DISCUSSION

The considered archival and original optical, UV and X-ray data indicate that J1944 is a tight binary accreting system with an orbital period of ≈ 1.5 hours. The orbital period is unambiguously determined from the analysis of time variations in the emission spectral lines of the hydrogen Balmer series, ionized and neutral helium. The double-peaked emission lines and the Doppler tomography also indicate the presence of an accretion disk and hot spots associated with the collisions of disk material with a stream of gas from the donor star overflowing its Roche lobe. Occasionally, a signature of the orbital period also appears in the optical light curves obtained from the multiband photometry and has one maximum per period. However, in most observations, the optical brightness varies stochastically on time scales ranging from minutes to hours, exhibiting sporadic flares at a level of a few tenths of a magnitude, observed simultaneously in several filters. This indicates that the accretion process is unstable. We found no evidence of eclipses in this binary system. At the same time, we discovered that occasionally, on scales of several months/years, J1944 abruptly transits into fairly long (from six months or more) high and low states, differing in optical brightness by more than one magnitude. Transitions occur simultaneously in X-rays, the optical and UV ranges, and they are likely associated with a significant change in the accretion rate. In the low state the optical light curves do not exhibit flare activity, but show regular variations in the emission intensity with a period of ≈ 8 min. In a high state the optical spectrum of the system is

almost completely dominated by the disk emission. At the same time, in the low state the spectral energy distributions in the optical and UV likely correspond to a stellar spectrum (see below).

The mentioned observational properties of J1944 are typical for a CV consisting of an accreting white dwarf and a non-degenerate late-type star, which is a donor of accreting material. The presence of an 8-min period excludes the interpretation of the object as a binary system with a neutron star, expected to be a millisecond pulsar. Assuming that J1944 is the CV, below we estimate the binary system’s parameters in detail, discuss their relevance to those expected for such objects and consider a possible CV type.

Masses of components and orbital parameters of the CV, temperature of the white dwarf

An estimate of the secondary component (donor) mass M_2 can be found from the requirement that it fills the Roche lobe. According to Sirotkin, Kim (2010) the effective radius of the Roche lobe R_L of the donor is related to the mass ratio $q = M_2/M_1$ by the expression

$$R_L = A \frac{0.5126q^{0.7388}}{0.6710q^{0.7349} + \ln(1 + q^{0.3983})}, \quad (3)$$

where A is the semi-major axis of the system, related to the masses of the components and the orbital period by Kepler’s third law $A = (M_2(1 + 1/q)P_{orb}^2)^{1/3}$, M_1 — mass of the accretor (white dwarf). Equation (3) is a refinement of the relation from Eggleton (1983) for polytropic stellar models (polytropic exponent $n = 3/2$), which reproduce better the fully convective donors in CVs below the orbital period gap. On the other hand, the radius of a star is evolutionarily related to its mass. We used the empirical relationship $R_2(M_2)$ presented in Knigge, Baraffe, et al. (2011) and shown in Fig. 14. It is approximated by two red lines. The first corresponds to donors with a mass $M_2 < 0.069M_\odot$ and the binary system evolves with increasing period (period bouncer). The second line is an approximation for masses $M_2 \in 0.069 - 0.20M_\odot$. The plot also shows the relation (3) of the Roche lobe radius (blue line), calculated for white dwarf masses $M_1 \in 0.2 - 1.44M_\odot$ (R_L weakly depends on M_1). From Fig. 14 it is clear that the donor radius is consistent with the radius of the Roche lobe at $M_2 \leq 0.08 \pm 0.01M_\odot$ which is the upper limit of the mass M_2 .

Top panel of Fig. 15 shows the solution in the $i - M_1$ plane (i is the inclination) corresponding to

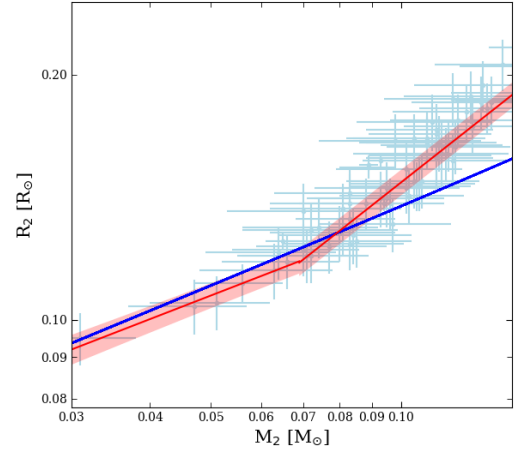


Fig. 14. The “radius – mass” relation for the donor in the CV. Data points and error bars correspond to measurements from Knigge (2006). Red lines are power-law approximations with the 1- σ uncertainties (pink polygons) for donors with masses $M_2 < 0.069 M_\odot$ (period bouncers) and $0.069 M_\odot < M_2 < 0.20 M_\odot$ obtained by Knigge (2006); Knigge, Baraffe, et al. (2011). The blue line points out the effective radii of the donor Roche lobe, calculated for the masses of the white dwarf $M_1 \in 0.20 - 1.44 M_\odot$.

the found radial velocity semi-amplitude K_1 for the donor mass upper limit $0.08M_\odot$. A decrease in the donor mass shifts this curve to the left, which leads to a decrease in the accretor mass (bottom panel of Fig. 15). The resulting solution for $i = 90^\circ$ gives a limit on the accretor mass $M_1 \lesssim 1.55 M_\odot$ that exceeds the Chandrasekhar limit for white dwarfs.

To reduce the range of acceptable system parameters, we estimated the velocity projection of the outer edge of the accretion disk $v_{out} \sin i$. According to Yakin, et al. (2013); Neustroev, et al. (2016), we assumed that the distance between the peaks in the emission lines (in velocity units) is equal to the velocity projection $v \sin i$ of the disk ring where the emission is formed. The spectral line intensity is sensitive to the local parameters of the accretion disk (temperature, pressure), and therefore the distance between the peaks of different lines corresponds to different rings of the disk. The minimum $v \sin i$ was calculated for the $H\alpha$ line and it is equal to $v \sin i \approx 465$ km/s. We accept this value as the estimate of $v_{out} \sin i$.

Assuming that the motion of particles at the outer edge of the disk is close to Keplerian, the projection of the rotation velocity is equal to

$$v_{out} \sin i = \left(\frac{GM_1}{R_{out}} \right)^{1/2} \sin i, \quad (4)$$

where R_{out} is the radius of the accretion disk. According to Paczynski (1977); Warner (1995), the

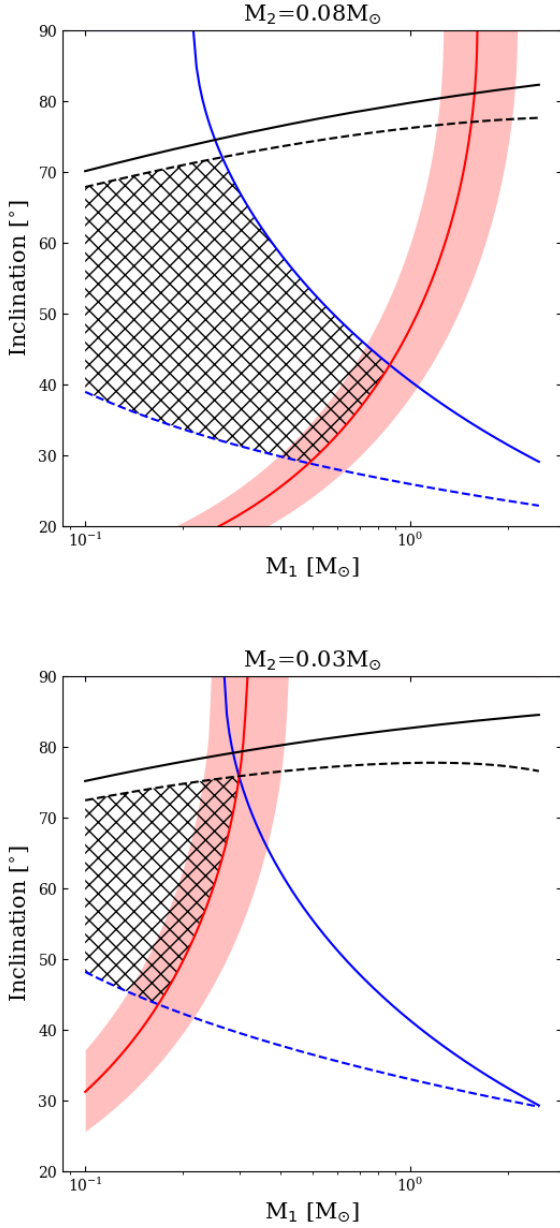


Fig. 15. Set of solutions in the $i - M_1$ plane. The solutions for the donor mass $M_2 = 0.08M_\odot$ are shown at the top, and for $M_2 = 0.03M_\odot$ at the bottom. The red solid lines are solutions that are derived from the white dwarf radial velocity semi-amplitude K_1 . Blue solid lines are solutions based on the assumption that the peaks of the $H\alpha$ lines form at the edge of the accretion disk of the maximum radius R_{\max} . Similar solutions for an accretion disk of the minimum radius R_{\min} are marked with blue dotted lines. The black solid line shows the inclinations i , at which the eclipse of the accretor occurs, and the black dotted line shows the inclinations up to which there is no eclipse of the accretion disk of radius R_{\min} .

size of the accretion disk R_{out} is limited by the tidal forces of the secondary component and is estimated by the formula

$$R_{\max} = A \frac{0.6}{1+q}. \quad (5)$$

The solution corresponding to this projection of the rotation velocity for $M_2 = 0.08M_\odot$ is plotted on the $i - M_1$ plane shown in the top panel of Fig. 15. As can be seen, for a donor mass $M_2 = 0.08M_\odot$ we have an accretor mass $M_1 \approx 0.88M_\odot$, consistent with the Chandrasekhar limit, and an orbital inclination $i \approx 43^\circ$. In Fig. 15, we also show restrictions on orbital inclination, due to the lack of eclipses in the system. The first restriction reflects the absence of an eclipse of the accretor, and the second – the accretion disk. For the last constraint, we used the relation for the minimum radius of the accretion disk from Hessman, Hopp (1990)

$$R_{\min} = 0.0859Aq^{-0.426}. \quad (6)$$

The bottom panel of Fig. 15 shows a solution set for a donor with the mass $M_2 = 0.03M_\odot$. The intersection of the solution curves obtained for K_1 and $v_{\text{out}} \sin i$ corresponds to the limiting orbital inclination i . At lower masses M_2 the system parameters are inconsistent with the absence of eclipses in J1944. Therefore, $M_2 = 0.03M_\odot$ can be considered as a lower limit for the donor mass. From Fig. 15 it follows that the accretor mass is in the range $M_1 \in 0.30 - 0.88M_\odot$, and the orbital inclination is in the range $i \in 40 - 75^\circ$. It should be noted that the restrictions on the accretor mass and orbital inclination are derived from the assumption that the $H\alpha$ line peaks form at the edge of the accretion disk. If they are formed in a ring of radius $R \in R_{\min} - R_{\max}$, then the range of permissible parameters of the system significantly expands. The regions of feasible solutions for two limiting donor masses are shown in Fig. 15 by shaded areas and are consistent with the values expected for CVs.

In 2023, the source J1944 transitioned to the low state with a brightness of $\langle g \rangle \approx 20^m$. In the optical and UV observations, the orbital variability of the object was absent. One can assume that in the low state the main source of radiation is the white dwarf. Based on that, we attempted to reproduce the spectral energy distribution of J1944 (Fig. 16) using spectra of hydrogen model atmospheres of white dwarfs calculated by Koester (2010). The fit was performed using the least squares method and based on the observed fluxes in the $uvw1$, $uvm2$, $uvw2$, g and r filters. The

flux errors in the g and r filters are equal to the approximate brightness variability 0.1^m of J1944 in the low state. The fluxes in the i and z filters were excluded due to a possible contribution of the accretion disk and donor. The flux in the u filter was excluded due to contamination from nearby stars. The J1944 photometric fluxes have been corrected for the interstellar extinction using the extinction curve from Fitzpatrick (1999). We used the color excess $E(B - V) = 0.06^m \pm 0.04^m$ for a distance of 415 pc in the source direction according to the interstellar extinction maps⁴ (Lallement, et al., 2014, 2018; Capitanio, et al., 2017). The extinction for J1944 in the Johnson V filter is $A_V = 3.1E(B - V) = 0.18^m$. The best fit of the spectral energy distribution was obtained for the white dwarf temperature $T = 14750 \pm 1250$ K. This temperature is typical for a CV below the period gap (Townsend, Gänsicke, 2009). The agreement with the observed fluxes is satisfied for the white dwarf radius $R_1 = 0.0094 - 0.0124R_\odot$, which corresponds to the mass $M_1 = 0.61 - 0.86M_\odot$ (Nauenberg, 1972). For details of the method for modeling the spectral energy distribution, we refer to Kolbin, et al. (2024). The resulting estimate of M_1 is consistent with its limitations presented above.

The low-mass donor is much cooler and its contribution is not evident in our data, but may be revealed in the red and infrared ranges of the spectrum. Observations in these ranges are necessary for its firm detection and classification.

As a result, our data and estimates show that the accretor is a white dwarf, and the donor is a low-mass star of a late spectral class, which confirms the CV nature of J1944.

Variability of radiation and periodicity

As previously noted, the J1944 can remain in the high and low states for several years. According to Fig. 4, the object was in the high state at least from July 2011 to December 2014 (3.4 years), then from March 2018 to December 2022 (4.7 years) and also from January to early May 2024 (0.5 years). The actual state of the source in the period from 2015 to 2017 could be clarified by the *Gaia* data, but at the moment the catalog contains only the averaged magnitude for all the observation period. J1944 was in the low state through 2023, and possibly between July 2005 and September 2010 (approximately 5.2 years), although the data is quite sparse. Currently the source has been in the low state since May 2024.

⁴<https://stilism.obspm.fr/>

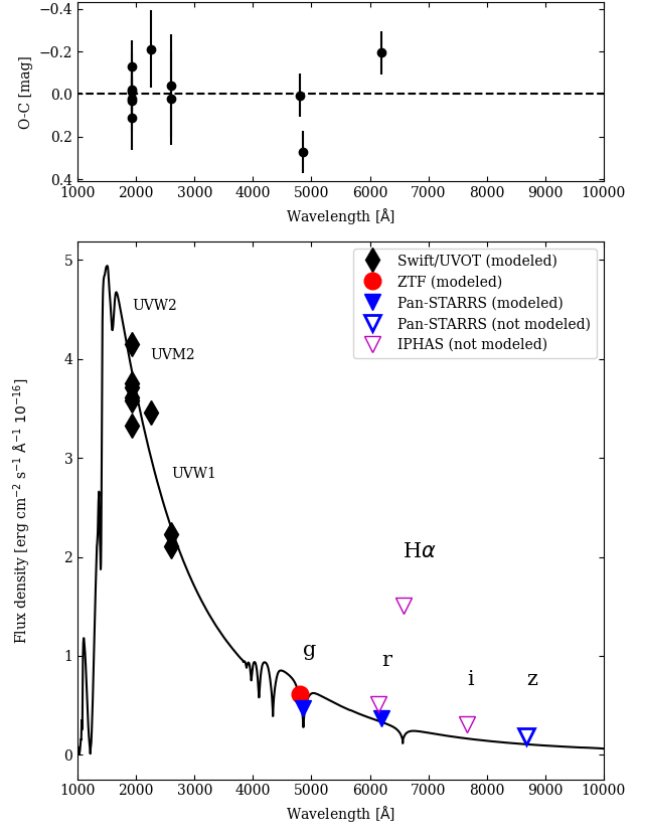


Fig. 16. The bottom panel shows the spectral energy distribution of J1944 in the low state constructed from the photometric data and the best-fitting model of the white dwarf. Filled symbols indicate the fluxes used to estimate atmospheric parameters; empty symbols were not taken into account. The residuals of the observed and simulated fluxes are shown in the top panel.

The photometric observations carried out with the RTT-150 telescope on June 15, 2024 resulted in the following magnitudes: $g = 19.82^m \pm 0.03^m$, $r = 19.82^m \pm 0.09^m$, $i = 19.76^m \pm 0.09^m$ and $z = 19.64^m \pm 0.07^m$. These values are in a good agreement with the Pan-STARRS, ZTF, and *Swift*/UVOT data obtained in the low state (see Fig. 4 and Table 3).

High and low states are observed in CV types such as polars (Mason, Santana, 2015), intermediate polars (Covington, et al., 2022; Mukai, Pretorius, 2023), and VY Scl-type nova-like systems (Honeycutt, Kafka, 2004). The presence of an accretion disk excludes the interpretation of the source as a polar.

The measured orbital period of the system $P = 89 \pm 1$ min is close to the minimum value of ~ 80 min for CVs with hydrogen donors (Knigge, 2006). Intermediate polars (Bernardini, et al., 2017)

have similar periods, while VY Scl type systems have longer periods, usually 3 – 6 hours (Medina Rodriguez, et al., 2023).

Short optical brightness variations with the period $P_s = 7.96$ min, that we derived from the photometric observations in 2023, when J1944 was in the low state, may be associated with the rotation of the white dwarf. This period is not detected in the high state of J1944, which is apparently due to the dominance of the accretion disk. If P_s is the real spin period of the white dwarf, then the ratio of the spin period to the orbital period $P_s/P = 0.09$ is close to the typical values of 0.01 – 0.1 for intermediate polars (Bernardini, et al., 2017).

On the other hand, P_s could be the pulsation period of the white dwarf (e.g., Szkody 2021). Estimates of mass and temperature indicate that our object may be in an instability strip. However, confirmation of an 8-min periodicity with a one sec accuracy from the photometric data of RTT-150 in 2024 is a strong argument in favor of the white dwarf spin. In addition, the observed amplitude of the 8-min brightness variability is 0.4^m . It significantly exceeds the observed amplitudes related with pulsations of white dwarfs, typically less than 0.2^m (see, e.g., Fontaine, Brassard 2008).

In the high state, only stochastic variations were detected on times of 1 – 15 min with amplitudes of $0.2 - 0.6^m$, and they were absent on smaller time scales.

X-ray spectra

The X-ray spectrum of J1944 can be described by a two-temperature optically thin plasma model, indicating temperature inhomogeneity of the emitting region. The derived temperatures are typical for CVs (e.g. Baskill, et al., 2005; Worpel, et al., 2020).

Using the color excess $E(B - V)$ for J1944 mentioned above and the empirical relation from Foight, et al. (2016), we estimated the hydrogen column density along the line of sight $N_H = (5.2 \pm 3.8) \times 10^{20} \text{ cm}^{-2}$. This is consistent with N_H obtained from the X-ray spectral analysis (see Table 4).

The estimated X-ray luminosities in the high and low states are $\approx 10^{32}$ and $\approx 10^{31} \text{ erg s}^{-1}$, respectively. The *XMM-Newton* scan of the source was performed on May 3, 2013, when J1944 was in the high state (see Fig. 4). The luminosity was ~ 2 times greater than in *Swift*/XRT observation data averaged over several years. Taking into account

the strong brightness variability of the source in the high state (Fig. 4), this is not surprising. The resulting X-ray luminosities are consistent with those of CVs with similar orbital periods (Mukai, Pretorius, 2023). The optical fluxes (calculated for the *g* band) in the high and low states are about 10 times lower than the X-ray fluxes in the respective states. This flux ratio is also typical for CVs (La Palombara, et al., 2006).

Accretion rate

Double-peaked emission lines are observed in the optical spectrum throughout the orbital period in the J1944 high state. This indicates the presence of an accretion disk, confirmed by the Doppler tomograms. In the high state, the white dwarf and the donor star are not revealed in the spectrum.

In the low state, the spectral energy distribution corresponds to the stellar one (Fig. 16). However, while the object was in the low state, from the IPHAS data the flux density in the $H\alpha$ line was three times greater than the continuum (this ratio is also observed for the high state). The presence of the emission line may be associated with accretion, which continues in the low state but at a significantly lower rate. The excess of the $H\alpha$ emission over the continuum is often observed for magnetic CVs in the low state (e.g. Kennedy, et al., 2020; Kolbin, et al., 2023). In this case, the continuum is dominated by the white dwarf emission. Strong emission lines formed in the disk are also present in the spectra of WZ Sge-type dwarf novae in a quiescent state (e.g. Amantayeva, et al., 2021).

We tried to estimate the accretion rate \dot{M} in the high and low states of J1944 assuming that all the energy produced by the accretion is mainly emitted in X-rays, using the formula

$$L_{X,\text{bol}} \sim \frac{GM_1\dot{M}}{2R_1}, \quad (7)$$

where $L_{X,\text{bol}}$ is the bolometric luminosity. Bolometric fluxes were obtained using the best fit to the X-ray spectra of J1944, $F_{X,\text{bol}}^h \sim 7 \times 10^{-12} \text{ erg s}^{-1} \text{ cm}^{-2}$ and $F_{X,\text{bol}}^l \sim 6 \times 10^{-13} \text{ erg s}^{-1} \text{ cm}^{-2}$. As a result, the accretion rate in the low state is

$$\dot{M}^l \approx 3 \times 10^{-12} \frac{R_1}{10^4 \text{ km}} \frac{M_\odot}{M_1} M_\odot \text{ yr}^{-1}, \quad (8)$$

while the accretion rate in the high state is an order of magnitude higher for any acceptable values from the mass M_1 and radius R_1 ranges of the white dwarf estimated above.

Type of the cataclysmic variable

As mentioned above, the presence of an accretion disk in J1944 excludes its classification as a (asynchronous) polar. Its properties are close to the VY Scl type CVs, which also demonstrate low and high states with typical flux variations in a range of 3 – 5^m. The main differences are that VY Scl systems have typical orbital periods of 3 – 6 hours (Medina Rodriguez, et al., 2023), white dwarf temperatures of more than 20,000 K, and the accretion rate in the high state by two orders of magnitude higher than for J1944. According to its characteristics, J1944 is most likely an intermediate polar.

The equivalent width ratio of HeII λ 4686/H β in the J1944 spectrum is less than the typical value >0.4 for magnetic CVs (Silber, 1992). However, there are intermediate polars with similar ratios, for example, DW Cnc⁵. This is also a short-period system ($P_{orb} = 86$ min) demonstrating high and low states (Duffy, et al., 2022).

*Association with the γ -ray source
4FGL J1943.9+2841*

J1944 is located in the error ellipse of the unidentified γ -ray source 4FGL J1943.9+2841, which raises the question of their possible association. γ -ray emission from CVs is extremely rarely detected. Only a few novae eruptions were observed in γ -rays (Sinitsyna, Sinitsyna, 2016; Sokolovsky, et al., 2022, 2023). Only for two rapidly rotating magnetic white dwarfs in binary systems, AE Aqr and AR Sco (the spin periods are 33 and 117 s, respectively), pulsations with the spin period of the white dwarf were possibly detected in the γ -rays (Meintjes, et al, 2023). AE Aqr is an intermediate polar with a magnetic field of $B \sim 10^6$ G, and AR Sco shows a number of properties that distinguish it from all known classes of CVs. The accretion rate in both systems is very low, an accretion disk is not formed: in AE Aqr – due to the propeller effect, in AR Sco – due to the strong magnetic field of the white dwarf ($B \sim 10^8$ G).

Classifying J1944 as a CV makes the association with 4FGL J1943.9+2841 very unlikely, since there are no signs of a nova, there is an accretion disk and there are no such peculiar properties as for AE Aqr.

Nevertheless, we note that 4FGL J1943.9+2841 still could be a pulsar. Further multi-wavelength studies are needed to confirm this hypothesis.

⁵The source spectrum is available in the LAMOST survey <https://www.lamost.org/dr8/v2.0/spectrum/view?obsid=392716175>

Conclusion

Our results show that J1944 has a number of characteristic features which allow us to classify it as an intermediate polar. It is remarkable that in this case it joins a small group of intermediate polars with the shortest orbital periods, lying below the period gap (Mukai, Pretorius, 2023), and exhibiting transitions between the high and low brightness states in the optical and X-rays. Currently, the low state has been detected in only eleven intermediate polars (e.g., Covington, et al., 2022; Mukai, Pretorius, 2023), and only two objects, FO Aqr and Swift J0746.3–1608 (Bernardini, et al., 2019), have been observed in X-rays in both the low and high states. Thus, the relatively bright source J1944 is a unique object for studying the evolution of similar systems simultaneously in the optical-UV and X-rays. Additional X-ray observations may reveal detailed information about the 8-min periodicity of the white dwarf emission. Optical-near-infrared spectroscopy of J1944 in the low state will allow one to significantly clarify the parameters of the white dwarf and, possibly, the donor star, as well as the parameters of the binary system.

Acknowledgments

This study used observations from the eROSITA telescope on board the SRG Observatory. The SRG observatory was manufactured by Roscosmos in the interests of the Russian Academy of Sciences represented by the Space Research Institute (IKI) within the framework of the Russian Federal Scientific Program with the participation of the German Aerospace Center (DLR). The X-ray telescope SRG/eROSITA was manufactured by a consortium of German institutes led by the Max Planck Institute for Extraterrestrial Astrophysics (MPE) with support from DLR. The SRG spacecraft was designed, manufactured, launched and managed by NPO Lavochkin and its subcontractors. Scientific data is received by a complex of deep space communication antennas in Bear Lakes, Ussuriysk and Baikonur and is financed by Roscosmos. The eROSITA telescope data used in this work were processed using eSASS software developed by the German eROSITA consortium and software developed by the Russian SRG/eROSITA telescope consortium.

This work made use of data supplied by the UK Swift Science Data Centre at the University of Leicester.

This work has made use of data from the European Space Agency (ESA) mission *Gaia* (<https://www.cosmos.esa.int/gaia>), processed by the *Gaia* Data Processing and Analysis Consortium (DPAC, <https://www.cosmos.esa.int/web/gaia/dpac/consortium>). Funding for the DPAC has been provided by national institutions, in particular the institutions participating in the *Gaia* Multilateral Agreement. Based on observations obtained with the Samuel Oschin Telescope 48-inch and the 60-inch Telescope at the Palomar Observatory as part of the Zwicky Transient Facility project. ZTF is supported by the National Science Foundation under Grants No. AST-1440341 and AST-2034437 and a collaboration including current partners

Caltech, IPAC, the Weizmann Institute for Science, the Oskar Klein Center at Stockholm University, the University of Maryland, Deutsches Elektronen-Synchrotron and Humboldt University, the TANGO Consortium of Taiwan, the University of Wisconsin at Milwaukee, Trinity College Dublin, Lawrence Livermore National Laboratories, IN2P3, University of Warwick, Ruhr University Bochum, Northwestern University and former partners the University of Washington, Los Alamos National Laboratories, and Lawrence Berkeley National Laboratories. Operations are conducted by COO, IPAC, and UW. The Pan-STARRS1 Surveys (PS1) and the PS1 public science archive have been made possible through contributions by the Institute for Astronomy, the University of Hawaii, the Pan-STARRS Project Office, the Max-Planck Society and its participating institutes, the Max Planck Institute for Astronomy, Heidelberg and the Max Planck Institute for Extraterrestrial Physics, Garching, The Johns Hopkins University, Durham University, the University of Edinburgh, the Queen's University Belfast, the Harvard-Smithsonian Center for Astrophysics, the Las Cumbres Observatory Global Telescope Network Incorporated, the National Central University of Taiwan, the Space Telescope Science Institute, the National Aeronautics and Space Administration under Grant No. NNX08AR22G issued through the Planetary Science Division of the NASA Science Mission Directorate, the National Science Foundation Grant No. AST-1238877, the University of Maryland, Eotvos Lorand University (ELTE), the Los Alamos National Laboratory, and the Gordon and Betty Moore Foundation.

This paper makes use of data obtained as part of the INT Photometric H α Survey of the Northern Galactic Plane (IPHAS, www.iphas.org) carried out at the Isaac Newton Telescope (INT). The INT is operated on the island of La Palma by the Isaac Newton Group in the Spanish Observatorio del Roque de los Muchachos of the Instituto de Astrofísica de Canarias. All IPHAS data are processed by the Cambridge Astronomical Survey Unit, at the Institute of Astronomy in Cambridge. The bandmerged DR2 catalogue was assembled at the Centre for Astrophysics Research, University of Hertfordshire, supported by STFC grant ST/J001333/1.

The authors are grateful to TUBITAK, IKI, KFU and the Tatarstan Academy of Sciences for partial support in the use of RTT-150 (Russian-Turkish 1.5-m telescope in Antalya). Observations at telescopes of the Special Astrophysical Observatory of the Russian Academy of Sciences are carried out with the support of the Ministry of Science and Higher Education of the Russian Federation. The renovation of telescope equipment is currently provided within the national project «Science and universities». Based upon observations carried out at the Observatorio Astronómico Nacional on the Sierra San Pedro Mártir (OAN-SPM), Baja California, México. We thank the daytime and night support staff at the OAN-SPM for facilitating and helping obtain our observations. The work was partially carried out within the framework of the state assignment of the Special Astrophysical Observatory of the Russian Academy of Sciences, approved by the Ministry of Science and Higher Education of the Russian Federation, as well as at the expense of the Strategic Academic Leadership Program of the Kazan (Volga Region) Federal University.

The work of IFB, IMH, MAG, ENI, MVS, RIG, NAS was carried out with the help of a subsidy from the Ministry of Education and Science of the Russian Federation

FZSM-2023-0015, allocated to Kazan Federal University to fulfill the state assignment in the field of scientific activity.

The work of YuAS, AVK and DAZ (analysis of archival optical, ultraviolet and X-ray data, as well as analysis of data from the 2.1-m OAN-SPM telescope and the eROSITA telescope) was carried out within the framework of the state assignment of the Ioffe Institute number FFUG-2024-0002. DAZ thanks the Pirinem School of Theoretical Physics for hospitality.

AYK acknowledges the DGAPA-PAPIIT grant IA105024 (planning optical observations with the OAN-SPM 2.1-m telescope and obtaining data).

The work of AIK (analysis of optical spectra, estimation of parameters of the binary system) was supported by the Russian Science Foundation grant No. 22-72-10064, <https://rscf.ru/project/22-72-10064/>.

REFERENCES

1. Abdollahi, et al. (S. Abdollahi, F. Acero, L. Baldini et al.), *Astrophys. J. Suppl. Ser.* **260**, 53 (2022).
2. Amantayeva, et al. (A. Amantayeva, S. Zharikov, K.L. Page et al.), *Astrophys. J.* **918**, 58 (2021).
3. Arnaud (K.A. Arnaud), *Astronomical Data Analysis Software and Systems V*, A.S.P. Conference Series **101**, 17 (1996).
4. Afanasiev, Moiseev (V.L. Afanasiev, A.V. Moiseev), *BaltA* **20**, 363 (2011).
5. Ballet, et al. (J. Ballet, P. Bruel, T.H. Burnett et al.), Preprint arXiv:2307.12546.
6. Barentsen, et al. (G. Barentsen, H.J. Farnhill, J.E. Drew et al.), *MNRAS.* **444**, 3230 (2014).
7. Baskill, et al. (D.S. Baskill, P.J. Wheatley, P. Julian), *MNRAS.* **357**, 626 (2005).
8. Bernardini, et al. (F. Bernardini, D. de Martino D., K. Mukai et al.), *MNRAS.* **470**, 4815 (2017).
9. Bernardini, et al. (F. Bernardini, D. de Martino, K. Mukai, M. Falanga), *MNRAS.* **484**, 101 (2019).
10. Boller, et al. (Th. Boller, M.J. Freyberg, J. Trümper et al.), *Astron. Astrophys.* **588**, A103 (2016).
11. Bailer-Jones, et al. (C.A.L. Bailer-Jones, J. Rybizki, M. Fouesneau, M. Demleitner, R. Andrae), *Astrophys. J.* **161**, 147 (2021).
12. Capitanio, et al. (L. Capitanio, R. Lallement, J.L. Vergely, M. Elyajouri, A. Monreal-Ibero), *Astron. Astrophys.* **606**, A65 (2017).
13. Cash (W. Cash), *Astrophys. J.* **228**, 939 (1979).
14. Covington, et al. (A.E. Covington, A.W. Shaw, K. Mukai et al.), *Astrophys. J.* **928**, 164 (2022).
15. Duffy, et al. (C. Duffy, G. Ramsay, D. Steeghs et al.), *MNRAS.* **510**, 1002 (2022).
16. Debur, et al. (Debur V., Arkhipova T., Beskin G.), *Nucl. Instrum. Methods Phys. Res.* **513(1-2)**, 127 (2003).
17. van Dokkum (P.G. van Dokkum), *PASP* **113**, 1420 (2001).

18. Eggleton (P.P. Eggleton), *Astrophys. J.* **268**, 368 (1983).
19. Evans, et al. (P.A. Evans, A.P. Beardmore, K.L. Page et al.), *MNRAS.* **397**, 1177 (2009).
20. Evans, et al. (P.A. Evans, K.L. Page, J.P. Osborne, et al.), *Astrophys. J. Suppl. Ser.* **247**, 54 (2020).
21. Fontaine, Brassard (G. Fontaine and P. Brassard), *PASP* **120**, 1043 (2008).
22. Fitzpatrick (E.L. Fitzpatrick), *PASP* **111**, 63 (1999).
23. Flewelling, et al. (H.A. Flewelling, E.A. Magnier, K.C. Chambers et al.), *Astrophys. J. Suppl. Ser.* **251**, 7 (2020).
24. Foight, et al. (D.R. Foight, T. Güver, F. Özel, P.O. Slane), *Astrophys. J.* **826**, 66 (2016).
25. *Gaia* Collaboration, et al. (*Gaia* Collaboration, T. Prusti, J.H.J. de Bruijne et al.), *Astron. Astrophys.* **595**, A1 (2016).
26. *Gaia* Collaboration, et al. (*Gaia* Collaboration, A. Vallenari, A.G.A. Brown et al.), *Astron. Astrophys.* **674**, A1 (2023).
27. Kennedy, et al. (M.R. Kennedy, P.M. Garnavich, C. Littlefield et al.), *MNRAS.* **495**, 4445 (2020).
28. Koester (D. Koester), *Memorie della Societa Astronomica Italiana* **81**, 921 (2010).
29. Knigge (C. Knigge), *MNRAS.* **373**, 484 (2006).
30. Knigge, Baraffe, et al. (C. Knigge, I. Baraffe, J. Patterson), *Astrophys. J. Suppl. Ser.* **194**, 28 (2011).
31. Kolbin, et al. (A.I. Kolbin, N.V. Borisov, A.N. Burenkov et al.), *Astron. Lett.* **49**, 129 (2023).
32. Kolbin, et al. (A.I. Kolbin, E.P. Pavlenko, V.Yu. Kochkina, et al.), *Astron. Lett.* **50**, ... (2024). (in print)
33. Kotze, et al. (E.J. Kotze, S.B. Potter, and V.A. McBride), *Astron. Astrophys.* **579**, 77 (2015).
34. Kotze, Potter, et al. (E.J. Kotze, S.B. Potter, V.A. McBride), *Astron. Astrophys.* **595**, 47 (2016).
35. La Palombara, et al. (N. La Palombara, R. P. Mignani, E. Hatziminaoglou et al.), *Astron. Astrophys.* **458**, 245 (2006).
36. Lallement, et al. (R. Lallement, J.-L. Vergely, B. Valette et al.), *Astron. Astrophys.* **561**, A91 (2014).
37. Lallement, et al. (R. Lallement, L. Capitanio, L. Ruiz-Dern et al.), *Astron. Astrophys.* **616**, A132 (2018).
38. Liedahl, et al. (D.A. Liedahl, A.L. Osterheld, W.H. Goldstein), *Astrophys. J. (Letters)* **438**, L115 (1995).
39. Marsh, Schwobe (T.R. Marsh, A.D. Schwobe), *ASSL* **439**, 195 (2016).
40. Masci, et al. (F.J. Masci, R.R. Laher, B. Rusholme et al.), *PASP* **131**, 018003 (2019).
41. Mewe, et al. (R. Mewe, E.H.B.M. Gronenschild, G.H.J. van den Oord), *Astron. Astrophys. Suppl. Ser.* **62**, 197 (1985).
42. Mewe, et al. (R. Mewe, J.R. Lemen, G.H.J. van den Oord), *Astron. Astrophys. Suppl. Ser.* **65**, 511 (1986).
43. Medina Rodriguez, et al. (Medina Rodriguez A. L., Zharikov S., Kára J., et al.), *MNRAS.* **521**, 5846 (2023).
44. Meintjes, et al. (P.J. Meintjes, S.T. Madzime, Q. Kaplan, H.J. van Heerden), *Galaxies* **11**, 14 (2023).
45. Mitsuda, et al. (K. Mitsuda, H. Inoue, N. Nakamura, Y. Tanaka), *PASJ* **41**, 97 (1989).
46. Mukai, Pretorius (K. Mukai, M.L. Pretorius), *MNRAS.* **523**, 3192 (2023).
47. Mason, Santana (P.A. Mason, J.B. Santana), *Proc. The Golden Age of Cataclysmic Variables and Related Objects III (Proc. of Science, v.255)*, 16 (2015).
48. Neustroev, et al. (V.V. Neustroev, S.V. Zharikov, N.V. Borisov), *Astron. Astrophys.* **586**, A10 (2016).
49. Nauenberg (M. Nauenberg), *Astrophys. J.* **175**, 417 (1972).
50. Nucita, et al. (A.A. Nucita, E. Kuulkers, F. De Paolis et al.), *Astron. Astrophys.* **566**, A121 (2014).
51. Oke (J.B. Oke), *Astron. J.* **99**, 1621 (1990).
52. Papitto, de Martino (A. Papitto, D. de Martino), In: *Bhattacharyya, S., Papitto, A., Bhattacharya, D. (eds) Millisecond Pulsars. Astrophysics and Space Science Library*, vol 465., pp 157–200. Springer, Cham. (2022).
53. Paczynski (B. Paczynski), *Astrophys. J.* **216**, 822 (1977).
54. Plokhotnichenko, et al. (Plokhotnichenko V.L., Beskin G.M., de Boer V.G., et al.), *Astrophysical Bulletin* **76(4)**, 472 (2021).
55. Plokhotnichenko, et al. (Plokhotnichenko V.L., Beskin G.M., de Boer V.G., et al.), *Bulletin of the Crimean Astrophysical Observatory* **119(3)**, 11 (2023).
56. Plokhotnichenko, et al. (Plokhotnichenko V.L., Solin A.V., Tikhonov A.G.), *Astrophysical Bulletin* **64(2)**, 198 (2009).
57. Predehl, et al. (P. Predehl, R. Andritschke, V. Arefiev, V. Babushkin, O. Batanov, W. Becker, H. Becker, H. Boehringer, et al.), *Astron. Astrophys.* **647**, A1 (2021).
58. Reis, et al. (R.C. Reis, P.J. Wheatley, B.T. Gänsicke, J.P. Osborne), *MNRAS.* **430**, 1994 (2013).
59. Silber (A.D. Silber), *Studies of an X-Ray Selected Sample of Cataclysmic Variables. PhD Thesis, Massachusetts Institute of Technology* (1992).
60. Sinitsyna, Sinitsyna (V.G. Sinitsyna, V.Y. Sinitsyna), *Journal of Physics: Conference Series* **718**, 052046 (2016).
61. Sirotkin, Kim (F.V. Sirotkin, W.-T. Kim), *Astrophys. J. Suppl. Ser.* **721**, 1356 (2010).
62. Sokolovsky, et al. (K.V. Sokolovsky, K.-L. Li, R.L. de Oliveira et al.), *MNRAS.* **514**, 2239 (2022).

63. Sokolovsky, et al. (K.V. Sokolovsky, T.J. Johnson, S. Buson et al.), *MNRAS*. **521**, 5453 (2023).
64. Saxton, et al. (R.D. Saxton, A.M. Read, P. Esquej et al.), *Astron. Astrophys.* **480**, 611 (2008).
65. Sunyaev, et al. (R. Sunyaev, V. Arefiev, V. Babyshkin, et al.), *Astron. Astrophys.* **656**, A132 (2021).
66. Takata, et al. (J. Takata, X.F. Wang, A. K. H. Kong, et al.), *Astrophys. J.* **936**, 134 (2022).
67. Townsley, Gänsicke (D.M. Townsley, B.T. Gänsicke), *Astrophys. J.* **693**, 1007 (2009).
68. Torres, et al. (D.F. Torres, T. Lin, F. Coti Zelati), *MNRAS*. **486**, 1019 (2019).
69. VanderPlas (J.T. VanderPlas), *Astrophys. J. Suppl. Ser.* **236**, 16 (2018).
70. Wilms, et al. (J. Wilms, A. Allen, R. McCray), *Astrophys. J.* **542**, 914 (2000).
71. Warner (B. Warner), *Cataclysmic Variable Stars* (Cambridge Univ. Press, Cambridge).
72. Worpel, et al. (H. Worpel, A.D. Schwope, I. Traulsen et al.), *Astron. Astrophys.* **639**, A17 (2020).
73. Honeycutt, Kafka (R.K. Honeycutt, S. Kafka), *Astrophys. J.* **128**, 1279 (2004).
74. Hessman, Hopp (F.V. Hessman, U. Hopp), *Astron. Astrophys.* **228**, 387 (1990).
75. Horne (K. Horne), *PASP* **98**, 609 (1986).
76. Shafter (A.W. Shafter), *Astrophys. J.* **267**, 222 (1983).
77. Szkody (P. Szkody), *Frontiers in Astronomy and Space Sciences* **8**, 184 (2021).
78. Yakin, et al. (D.G. Yakin, V.F. Suleimanov, V.V. Vlasyuk, et al.), *Astron. Lett.* **39**, 38 (2013).